J Physiol 594.15 (2016) pp 4193–4224

The Journal of Physiology

The calcium–frequency response in the rat ventricular myocyte: an experimental and modelling study

Sara Gattoni[1], Åsmund Treu Røe[2,3], Michael Frisk[2,3], William E. Louch[2,3], Steven A. Niederer[1] and Nicolas P. Smith[1,4]

[1] *King's College London, Department of Biomedical Engineering and Imaging Sciences, St. Thomas' Hospital, London, UK*
[2] *Institute for Experimental Medical Research, Oslo University Hospital and University of Oslo, Oslo, Norway*
[3] *K. G. Jebsen Cardiac Research Center and Center for Heart Failure Research, University of Oslo, Oslo, Norway*
[4] *University of Auckland, Engineering School Block 1, Level 5, 20 Symonds St, Auckland 101, New Zealand*

Key points

- In the majority of species, including humans, increased heart rate increases cardiac contractility. This change is known as the force–frequency response (FFR). The majority of mammals have a positive force–frequency relationship (FFR). In rat the FFR is controversial.
- We derive a species- and temperature-specific data-driven model of the rat ventricular myocyte.
- As a measure of the FFR, we test the effects of changes in frequency and extracellular calcium on the calcium–frequency response (CFR) in our model and three altered models.
- The results show a biphasic peak calcium–frequency response, due to biphasic behaviour of the ryanodine receptor and the combined effect of the rapid calmodulin buffer and the frequency-dependent increase in diastolic calcium.
- Alterations to the model reveal that inclusion of Ca^{2+}/calmodulin-dependent protein kinase II (CAMKII)-mediated L-type channel and transient outward K^+ current activity enhances the positive magnitude calcium–frequency response, and the absence of CAMKII-mediated increase in activity of the sarco/endoplasmic reticulum Ca^{2+}-ATPase induces a negative magnitude calcium–frequency response.

Abstract An increase in heart rate affects the strength of cardiac contraction by altering the Ca^{2+} transient as a response to physiological demands. This is described by the force–frequency response (FFR), a change in developed force with pacing frequency. The majority of mammals, including humans, have a positive FFR, and cardiac contraction strength increases with heart rate. However, the rat and mouse are exceptions, with the majority of studies reporting a negative FFR, while others report either a biphasic or a positive FFR. Understanding the differences in the FFR between humans and rats is fundamental to interpreting rat-based experimental findings in the context of human physiology. We have developed a novel model of rat ventricular electrophysiology and calcium dynamics, derived predominantly from experimental data recorded under physiological conditions. As a measure of FFR, we tested the effects of changes in stimulation frequency and extracellular calcium concentration on the simulated Ca^{2+} transient characteristics and showed a biphasic peak calcium–frequency relationship, consistent with recent observations of a shift from negative to positive FFR when approaching the rat physiological frequency range. We tested the hypotheses that (1) inhibition of Ca^{2+}/calmodulin-dependent protein kinase II (CAMKII)-mediated increase in sarco/endoplasmic reticulum Ca^{2+}-ATPase (SERCA) activity, (2) CAMKII modulation of SERCA, L-type channel and transient outward K^+ current activity

DOI: 10.1113/JP272011

and (3) Na^+/K^+ pump dynamics play a significant role in the rat FFR. The results reveal a major role for CAMKII modulation of SERCA in the peak Ca^{2+}–frequency response, driven most significantly by the cytosolic calcium buffering system and changes in diastolic Ca^{2+}.

(Received 8 December 2015; accepted after revision 22 February 2016; first published online 25 February 2016)

Corresponding author N. P. Smith: King's College London, Department of Biomedical Engineering and Imaging Sciences, St Thomas' Hospital, The Rayne Institute, 4th floor North Wing, London SE1 7EH, UK. Email: nicolas.smith@kcl.ac.uk

Abbreviations AP, action potential; CaB, background Ca^{2+}; CAMKII, Ca^{2+}/calmodulin-dependent protein kinase II; CFR, calcium frequency response; DCFR, diastolic calcium frequency response; I_{to}, transient outward K^+ current; LCC, L-type Ca^{2+} channel; LV, left ventricle; FFR, force–frequency response; MCFR, magnitude calcium–frequency response; NCX, Na^+/Ca^{2+} exchanger; PCFR, peak calcium–frequency response; RyR, ryanodine receptor; PMCa, plasma membrane Ca^{2+}-ATPase; SERCA, sarco/endoplasmic reticulum Ca^{2+}-ATPase; SRl, SR leak; TRPN, troponin buffer.

Introduction

In the majority of species, including humans, increased heart rate increases cardiac contractility and the rate of relaxation (Pieske *et al.* 1999). This change in response to changes in pacing frequency, known as the force–frequency response (FFR), is described as either positive or negative with increasing or decreasing myocyte contraction strength, respectively, with increasing pacing frequencies. As an essential self-regulatory mechanism, FFR allows the cardiac output to respond to systemic requirements through coordinated changes in heart rate and contraction strength.

Key to understanding the cardiac FFR are the physiological mechanisms that regulate calcium handling in the heart. With each heartbeat, cardiomyocytes are depolarized, activating the voltage-dependent L-type Ca^{2+} channels (LCCs) that, in turn, induce an influx of Ca^{2+} (Hobai & Levi, 1999). The Ca^{2+} entering the cell signals the opening of the intracellular Ca^{2+} release channels known as ryanodine receptors (RyRs) in the sarcoplasmic reticulum (SR) (Fabiato & Fabiato, 1979), allowing rapid Ca^{2+}-induced Ca^{2+}-release to occur (Sham *et al.* 1995). The release of Ca^{2+} from the intracellular calcium stores results in a rapid increase in the cytosolic Ca^{2+} concentration, which is sufficient to generate contraction at the level of the myofilaments. During the relaxation phase, Ca^{2+} ions are sequestered back into the SR by the sarco/endoplasmic reticulum Ca^{2+}-ATPase (SERCA) or driven out the cell by the Na^+/Ca^{2+} exchanger (NCX) and the sarcolemma Ca^{2+}-ATPase (PMCa), returning Ca^{2+} concentration to low diastolic levels. FFR manifests at the cellular scale where contraction, Ca^{2+} transients and action potentials (APs) in isolated myocytes adapt in response to changes in pacing frequency (Endoh, 2004; Dibb *et al.* 2007; Monasky & Janssen, 2009). Specifically changes in the intracellular Ca^{2+} ($[Ca^{2+}]_i$) handling mechanism are the primary cellular responses that, in turn, produce the FFR (Endoh, 2004). Humans have a positive FFR (Pieske *et al.* 1999), while in the rat, the majority of murine studies have reported a negative FFR (Bers, 1989; Bouchard & Bose, 1989) and only a few studies have described a biphasic or positive FFR (Frampton *et al.* 1991*b*; Layland & Kentish, 1999). Central to this controversy are the physiological conditions under which the rat heart operates, specifically the heart rate, the temperature and the extracellular calcium concentration ($[Ca^{2+}]_o$).

The relative importance of the mechanisms regulating the FFR has been debated for more than a century and remains a source of controversy. Early works in the rat found a negative FFR at physiological frequencies in ventricular strips maintained at 38°C (Benforado, 1958). These responses were attributed to changes in intracellular sodium concentration ($[Na^+]_i$) with pacing frequency. With the discovery of the Na^+/Ca^{2+} exchanger (NCX), Langer *et al.* (1975) suggested that, following a $[Na^+]_i$ increase with frequency, increases in force may be generated by the coupled gain of intracellular calcium via NCX, thus shifting attention to the Ca^{2+}–frequency relationship (CFR) as a measure of FFR. Later experiments by Stemmer & Akera (1986) rejected this hypothesis and proposed that frequency-dependent $[Ca^{2+}]_i$ changes could be caused by a decrease in intracellular Ca^{2+} resulting from a reduction in Ca^{2+} available for release from the SR ($[Ca^{2+}]_{SR}$). This hypothesis was further tested in rats by Bers (1989) who attributed a negative FFR to a decrease in $[Ca^{2+}]_{SR}$ with increasing frequency.

In conflict with these results, Frampton *et al.* (1991*b*) showed a positive FFR, positive CFR and an increase in $[Ca^{2+}]_{SR}$ with frequency in isolated rat ventricle myocytes at room temperature. A frequency-dependent loading of the SR was also reported by Layland & Kentish (1999) in isolated rat ventricular trabeculae and Dibb *et al.* (2007) in isolated rat ventricular myocytes. In particular, Layland's results support the hypothesis that a shift from negative to positive FFR occurs as the pacing frequency approaches physiological rates, first noted by Koch-Weser & Blinks (1963).

Recent studies have suggested that the Ca^{2+}/calmodulin-dependent protein kinase II (CaMKII) contributes to enhanced activity of the target proteins that control the FFR (Sossalla *et al.* 2010; Wu *et al.* 2012) such as the sarco/endoplasmic reticulum Ca^{2+}-ATPase, the L-type channel and the transient outward K^+ current I_{to}, although other studies contradict this hypothesis (Lokuta *et al.* 1995; Dibb *et al.* 2007). What is now widely accepted and validated through experiments is that CAMKII indirectly enhances SR uptake of Ca^{2+} through SERCA by phosphorylation of the endogenous inhibitor of SERCA, phospolambam, inducing a frequency-dependent acceleration of relaxation (Picht *et al.* 2007; Dibb *et al.* 2007). Other experiments have also revealed CAMKII-mediated facilitation of the L-type Ca^{2+} current (Xiao *et al.* 1994) and the transient outward potassium current (Colinas *et al.* 2006). The effects of CaMKII phosphorylation of the RyRs, however, remain controversial as CAMKII has been reported to both increase (Wehrens *et al.* 2004) and decrease (Lokuta *et al.* 1995) the channel open probability.

This evidence collectively confirms that FFR regulation in rats still remains controversial and the mechanisms are not clear. Ca^{2+} dynamics are directly responsible for changes in FFR (Endoh, 2004) and in rats they appear to be different from canine, guinea pig and human as their rate relies more on intracellular calcium cycling than the other species. Thus, to be able to unravel the causes of positive and negative FFR we need to consider the rat-specific Ca^{2+} physiology. In this context, the development of a species- and temperature-specific model of Ca^{2+} dynamics in the cardiac myocyte, which integrates multiple data sources and can operate at physiological frequencies, provides a novel and promising methodology for quantitatively interpreting experimental data and quantifying the principal regulators of FFR in rats.

This study adopts this approach to focus on understanding FFR in rats. Firstly, we derive a species- and temperature-specific model of the rat ventricular myocyte electrophysiology that captures the change in Ca^{2+} response to pacing. Secondly, to study the FFR, we test the effects of changes in pacing frequency and $[Ca^{2+}]_o$ on the Ca^{2+} transient characteristics in a model with (1) CAMKII SERCA inhibition, (2) CAMKII modulation of SERCA, LCC and transient outward K^+ current (I_{to}) activity and (3) reduced Na^+/K^+ activity to quantify the relative role of those mechanisms in the response.

Methods

Ethical approval

Experiments were performed in healthy Wistar rats at physiological temperature (37°C). Ten-week-old Wistar rats were anaesthetized by inhalation of 2% isoflurane–98% oxygen in a chamber, and then killed by cervical dislocation. Animal experiments were approved by the Norwegian National Animal Research Committee and conformed to the *Guide for the Care and Use of Laboratory Animals* (National Institutes of Health, USA, publication no. 85-23, revised 1996) and the principles of UK regulations, as described in Drummond (2009).

Isolation of myocytes

Left ventricle (LV) myocytes were isolated using a standard enzymatic dispersion technique (Louch *et al.* 2011). The heart was perfused with a Ca^{2+}-free solution (mM: 130 NaCl, 25 Hepes, 5.4 KCl, 0.5 $MgCl_2$, 0.4 NaH_2PO_4, 5.5 D-glucose; pH 7.4) followed by 15 min with an enzyme-containing solution (collagenase, 1 mg ml^{-1}, Worthington Biochemical Corp., Lakewood, NJ, USA; Ca^{2+}: 0.05 mM). The LV free wall was isolated, cut into small pieces and gently minced. Isolated cardiomyocytes were allowed to sediment several times while Ca^{2+} concentration was gradually increased (0.1, 0.2, 0.5 mM). The myocyte suspension was stored at room temperature, and cells were used within 8h of isolation.

Ca^{2+} measurements

LV myocytes were plated on laminin-coated coverslips, and placed in a perfusion chamber on the stage of an inverted microscope. $[Ca^{2+}]_i$ transients were recorded in fluo-4 AM-loaded (Molecular Probes; Thermo Fisher Scientific, Waltham, MA, USA) myocytes during field stimulation at 1 and 6 Hz during superfusion with Hepes–Tyrode solution containing (in mM): 140 NaCl, 1.8 $CaCl_2$, 0.5 $MgCl_2$, 5.0 Hepes, 5.5 glucose, 0.4 NaH_2PO_4 and 5.4 HCl (pH 7.4, 37°C). The fluorescence measurements were converted to free $[Ca^{2+}]_i$ prior to their use. The conversion was developed using the following equation proposed by Cheng *et al.* (1993):

$$[Ca^{2+}]_i = \frac{K_d R}{\frac{K_d}{[Ca^{2+}]_d} - R + 1}, \qquad (1)$$

where $[Ca^{2+}]_i$ is the free Ca^{2+} concentration in the cytosol, $[Ca^{2+}]_d$ is the diastolic Ca^{2+} concentration at 1 Hz, K_d is the dissociation constant, and R is the fluorescence divided by diastolic fluorescence at 1 Hz (F/F_0). K_d was set to 1100 nM and $[Ca^{2+}]_d$ to 100 nM.

Patch-clamp experiments

Whole-cell patch-clamp experiments were performed with patch pipettes (1–2 MΩ) connected to an Axoclamp-2B amplifier (Axon Instruments/Molecular

Devices, Sunnyvale, CA, USA). Action potential recordings were performed as described in Mørk *et al.* (2009), with a pipette solution containing (in mM): 120 potassium aspartate, 0.5 $MgCl_2$, 6 NaCl, 0.06 EGTA, 10 Hepes, 10 glucose, 25 KCl and 4 K_2-ATP (pH 7.2), and an identical extracellular solution as described for field stimulation experiments. Action potentials were triggered by a 3 ms suprathreshold current.

For recordings of L-type Ca^{2+} current, the fast transient outward K^+ currents were blocked by the presence of aminopyridine and Cs^+ (Frisk *et al.* 2014). The intracellular solution contained (in mM): 133 CsCl, 0.33 $MgCl_2$, 4 Mg-ATP, 10 Hepes and 20 TEA, while the extracellular solution contained (in mM): 20 CsCl, 1 $MgCl_2$, 135 NaCl, 10 Hepes, 10 D-glucose, 4-aminopyridine and 1 $CaCl_2$. The additional presence of 0.06 mM of EGTA in the intracellular solution implies some Ca^{2+} buffering. Current was recorded during discontinuous voltage clamp (sample rate ∼8 Hz), with a train of 10 conditioning pulses (50 ms) from –70 to 0 mV, followed by a 210 ms depolarizing voltage step to a range of potentials (–40 to +40 mV in 10 mV increments). The peak inward current for each test potential was measured relative to steady-state current, and normalized to cellular capacitance. Cell capacitance was measured by integrating the capacitive current elicited by a voltage step from −70 mV to −80 mV.

Computational methods

Model structure. The importance of species and temperature specificity in heart modelling has recently been highlighted in a number of published studies (Li *et al.* 2010). Starting with the Pandit model of rat ventricular myocyte electrophysiology (Pandit *et al.* 2001), we created a phylogenetic tree to analyse the dependence of model parameters on experimental data (Fig. 1*A*). Specifically, the tree shows the link between model components and the modelling and experimental studies used to determine the parameters involved in that component's formulation. This approach identifies the Ca^{2+} handling system and Na^+/K^+ model as being derived predominantly from canine and guinea pig data. Based on this analysis and due to the lack in graded Ca^{2+} release of the Pandit model, we replaced the Ca^{2+} dynamics system with the Hinch model (Hinch *et al.* 2004) and we updated the Na^+/K^+ model by replacing it with the more recent Lewalle model (Lewalle *et al.* 2014), fitted to rat data at 37°C. The Hinch model phylogenetic tree is presented in Fig. 1*B*, highlighting data from species other than rat and rat data at temperatures lower than physiological. Based on this analysis we thus refitted the Ca^{2+} dynamics parameters and channel densities using MATLAB (The MathWorks, Natick, MA, USA) fitting tools (nonlinear least squares method with Trust-Region algorithm) to update data dependencies. In particular, we simulated and constrained six key proteins in the Ca^{2+} regulation system: the Na^+/Ca^{2+} exchanger current (I_{NCX}), the Ca^{2+} pump current (I_{PMCa}), the sarco/endoplasmic reticulum Ca^{2+}-ATPase current (I_{SERCA}), the L-type Ca^{2+} current (I_{LCC}), the ryanodine receptor current (I_{RYR}) and the leak from the SR current (I_{SRl}). We introduced equations for CAMKII-mediated increase in SERCA activity from the model of Li *et al.* (2010). To account for the presence of EGTA in the patched pipettes generating our experimental data, we included a model of EGTA buffering. Hence, the Ca^{2+} transient simulations were conducted using [EGTA] = 0 mM, while the AP simulations were performed with [EGTA] = 0.06 mM, consistent with the experimental methods.

Model parameter fitting. The fluxes through NCX and PMCa were evaluated using caffeine-induced Ca^{2+} transients at 1 and 6 Hz. NCX parameters were fitted in order for the pump to extrude 90% of the measured Ca^{2+} flux during a caffeine transient, while the remaining 10% was used to fit PMCa parameters. Those results were then combined with Ca^{2+} transient measurements at 1 and 6 Hz to study the Ca^{2+} flux of SERCA and its changes with frequency. The Ca^{2+} influx from the LCCs was fitted using the peak I_{LCC} current–voltage relationship curve, where peak I_{LCC} is the maximum value of I_{LCC}. The flux through the RyR was modulated to match the time to peak of the field simulated Ca^{2+} transients. The leak from the SR was fitted to constrain the $[Ca^{2+}]_{SR}$ to fall within the maximum value defined by the integral of NCX during a caffeine transient and the minimum value defined by the integral of SERCA during a field simulated Ca^{2+} transient. The background Ca^{2+} current was modified to reproduce the peak of the Ca^{2+} transients at 1 and 6 Hz. The remaining Na^+ and K^+ currents were modified using rat data recorded at physiological temperatures. The resulting coupled rat ventricular myocyte calcium dynamics and electrophysiology model's data dependences are shown in Fig. 1*C*, whereas the fitted parameters' values are shown in section 1.2.7 of Appendix. The model's coupling and refitting procedure is also described in detail in section 1 of Appendix.

Generation of model variants to simulate specific mechanisms. Using this data-driven species- and temperature-specific rat electrophysiology model (the DD model), we developed three model variants to analyse how CAMKII-mediated SERCA, L-type channel and I_{to} alterations (CAMK model), inhibition of CAMKII increase in SERCA activity (NO CAMK model) and altered Na^+/K^+ (RNaK model) affect the Ca^{2+} transient at different frequencies and $[Ca^{2+}]_o$ (see Fig. 3).

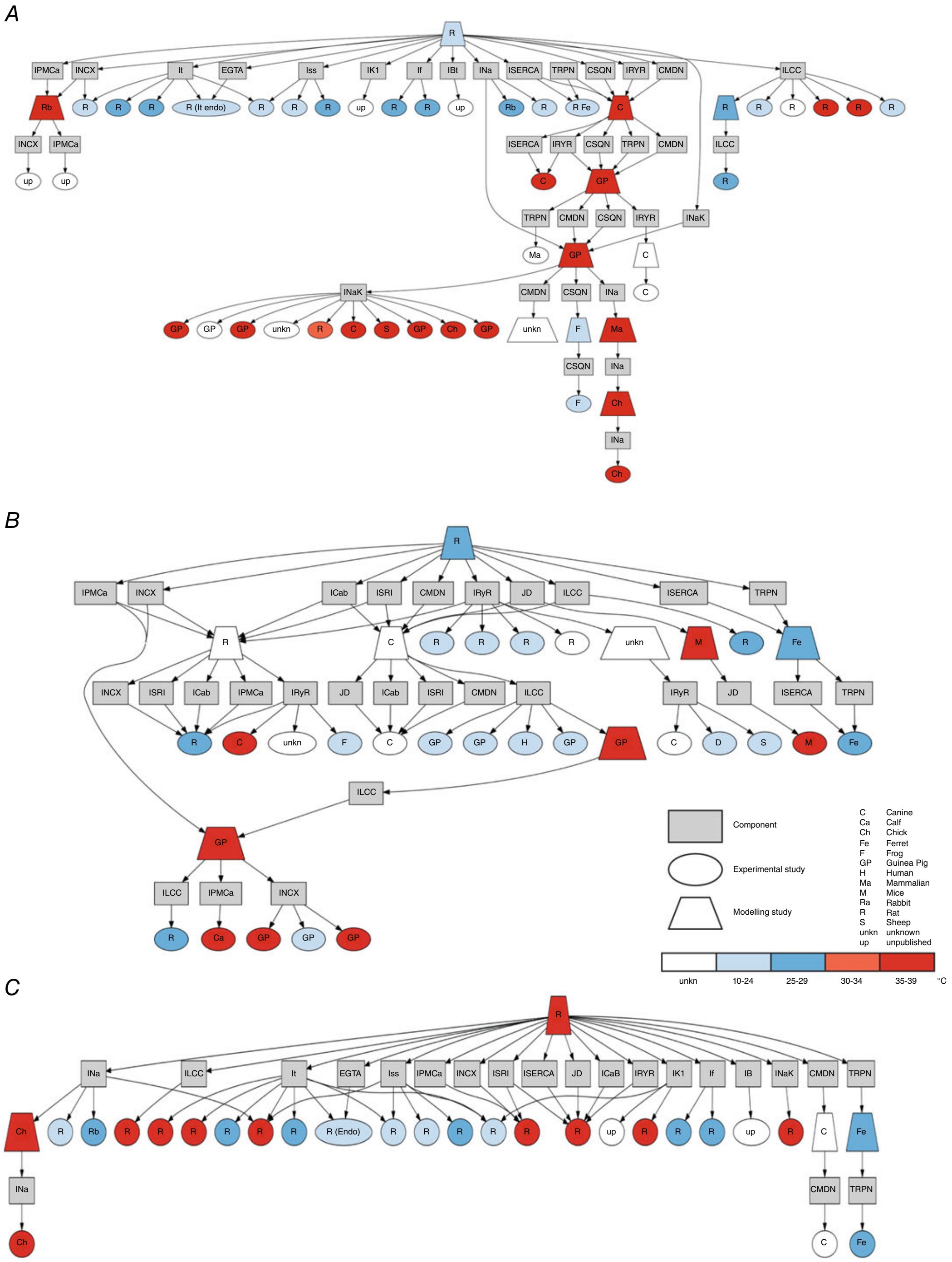

Figure 1. Phylogenetic trees

The figures show an analysis conducted on the transmembrane currents and the Ca^{2+} dynamics system showing the inheritance of data as links between modelling studies (trapezium) and experimental studies (ellipses). Modelling studies components (boxes) are connected (arrows) to published studies. Models and experiments within the trees are classified by species (label) and temperature (colour). The observed model's components are: L-type Ca^{2+} channel current (I_{LCC}), SR Ca^{2+}-ATPase current (I_{SERCA}), troponin buffer (TRPN), calsequestrin buffer (CSQN), flux from the dyadic space to the cytosol (J_D), ryanodine receptor current (I_{RYR}), calmodulin buffer (CMDN), Ca^{2+} pump current (I_{PMCa}), Na^+/Ca^{2+} exchanger current (I_{NCX}), EGTA buffer (EGTA), steady-state outward K^+ current (I_{ss}), inwardly rectifying K^+ current (I_{K1}), hyperpolarization-activated current (I_f), background Na^+, K^+ and Ca^{2+} currents (I_{Bt}, in *A*), background Na^+ and K currents (I_B in *B* and *C*), background Ca^{2+} current (I_{CaB} in *B* and *C*), SR leak current (I_{SRl}), Na^+ current (I_{Na}), Na^+/K^+ pump (I_{NaK}). *A*: Pandit phylogenetic tree. *B*: Hinch phylogenetic tree. *C*: new model phylogenetic tree.

In the DD model, CAMKII modulation of SERCA was already included, as it was required to allow the model to fit the distinct Ca^{2+} relaxation rates at 1 and 6 Hz due to changes in SERCA flux. It must be noted that L-type measurements were not performed at different frequencies and so do not provide a frequency-dependent response and no measurements of I_{to} were performed in our study.

As previous studies in the literature have reported CAMKII-mediated facilitation of the L-type Ca^{2+} (Xiao *et al.* 1994) and I_{to} (Colinas *et al.* 2006) currents, in the CAMK model we included CAMKII modulation of the L-type channel and I_{to}. The LCC and I_{to} models were fitted using CAMKII data in the literature, collected in rats and mice (for further details see section 5 of Appendix).

In the NO CAMK model we inhibited CAMKII activation of SERCA, by fixing the SERCA conductivity parameter value at 6 Hz for all the frequencies, to test the effect of increased SERCA activity on the CFR. This choice was forced by the development of alternans for frequencies > 4 Hz when fitting the SERCA conductivity at 1 Hz and is discussed in section 6.2 of Appendix.

In the RNaK model we reduced Na^+/K^+ affinity to Na^+. Results in Lewalle *et al.* (2014) have showed an increase in the Na^+/K^+ pump affinity to Na^+ in rats relative to the affinity in guinea pigs. To test the effect of this increase on the CFR we reduced the Na^+/K^+ affinity to Na^+ and we altered the maximum I_{NaK} current parameter, $I_{NaK,max} = 0.0002\ \mu A$, to obtain an intracellular Na^+ concentration of around 10 mM, comparable to results at 37°C performed by Harrison *et al.* (1992) in rats at 1 Hz (for further details see section 1.1.4 of Appendix).

Simulated phenotypes for comparison to experimental data. Previous studies tested the CFR response in rats by observing the peak systolic $[Ca^{2+}]_i$ (peak $[Ca^{2+}]_i$), diastolic $[Ca^{2+}]_i$ (DCa) and magnitude of peak $[Ca^{2+}]_i$ (MPCa = peak $[Ca^{2+}]_i$ − DCa) fluorescence ratios (Frampton *et al.* 1991*b*; Layland & Kentish, 1999). In our work, we simulated the peak $[Ca^{2+}]_i$ frequency response (PCFR), the diastolic $[Ca^{2+}]_i$ frequency response (DCFR), the magnitude of peak $[Ca^{2+}]_i$ frequency response (MCFR) and the $[Ca^{2+}]_{SR}$ frequency response, due to changes in $[Ca^{2+}]_o$. $[Ca^{2+}]_o$ was varied from 1 to 2 mM with 0.2 mM steps. An extracellular concentration of 2 mM did not allow AP repolarization, generating alternans at all frequencies, and so was not considered for analysis. Measurements were conducted at steady state, varying frequency from 1 to 6 Hz with 1 Hz steps. Results of the peak $[Ca^{2+}]_i$, DCa, relative change of the magnitude (Δ_{MPCa}) and $[Ca^{2+}]_{SR}$ frequency-dependent changes with $[Ca^{2+}]_o$ are shown in Fig. 3. Here, the relative change of the magnitude, for each frequency *i*, is defined as:

$$\Delta_{MPCa} = \frac{MPCa\,(i) - \overline{MPCa}}{\overline{MPCa}}, \tag{2}$$

where $\overline{MPCa} = \frac{1}{N}\sum_{i=1}^{N} MPCa(i)$ and N is the number of tested frequencies.

Results

Comparison between model results and experimental data

The final DD model shows close agreement between simulations and experimental data (see Fig. 2). The simulated Ca^{2+} transients, fitted to representative traces at 1 and 6 Hz, were in close agreement with the experimental data in rat ventricular myocytes at 37°C as shown in Fig. 2*G* and *H*. Comparisons of modelling simulations against experimental measurements of peak $[Ca^{2+}]_i$, DCa, time to 50% relaxation of the $[Ca^{2+}]_i$ transient (RT_{50}) and time to peak $[Ca^{2+}]_i$ (T_{peak}) at both 1 and 6 Hz are summarized in Table 1.

To validate the model, we measured the ratio of Ca^{2+} extrusion via SERCA, NCX and PMCa at 1 Hz and found those to be 88.9%, 9.5% and 1.6%, respectively. This compares well to measurements of 87–92%, 7.5–9% and 1–3.7% observed experimentally (Bassani *et al.* 1992; Negretti *et al.* 1993; Choi & Eisner, 1999; Mackiewicz & Lewartowski, 2006). The simulated AP is also comparable with the experimental observations at 1 and 6 Hz. Figure 2*I* and *J* shows the modelled AP superimposed to the available experimental measurements in one cell at 1 Hz and three different cells at 6 Hz. The simulated and experimentally measured AP characteristics are summarized in Table 2 where we show values for: resting membrane voltage, peak voltage, peak dV/dt, action potential duration at 20% repolarization (APD20), 50% repolarization (APD50), 70% repolarization (APD70) and 90% repolarization (APD90). Calcium and AP characteristics at all tested frequencies from 1 to 6 Hz are shown in section 2 of Appendix.

CFR response in rats at physiological temperature

Using our species- and temperature-specific rat electrophysiology model, we observed the CFR response for the DD, CAMK, NO CAMK and RNaK models. The results of our study are reported in Fig. 3 and show the simulated rate-dependent changes in peak $[Ca^{2+}]_i$, DCa, Δ_{MPCa} and $[Ca^{2+}]_{SR}$ due to changes in $[Ca^{2+}]_o$ in the four developed models. For completeness, phenotypes changes with frequency in all model variants are also reported in Table 12 (Appendix).

The PCFR in the DD model shows biphasic behaviour with frequency, with a negative staircase in the range 1 Hz to 2 or 3 Hz and a positive staircase in the range 2 or 3 Hz to 6 Hz, depending on $[\mathrm{Ca}^{2+}]_\mathrm{o}$. The same PCFR response is also visible in the RNaK model. In the CAMK model we see a positive PCFR at $[\mathrm{Ca}^{2+}]_\mathrm{o} = 1.8$ mM and the same biphasic response as the DD model at lower $[\mathrm{Ca}^{2+}]_\mathrm{o}$, while in the NO CAMK model we see a shift of the biphasic

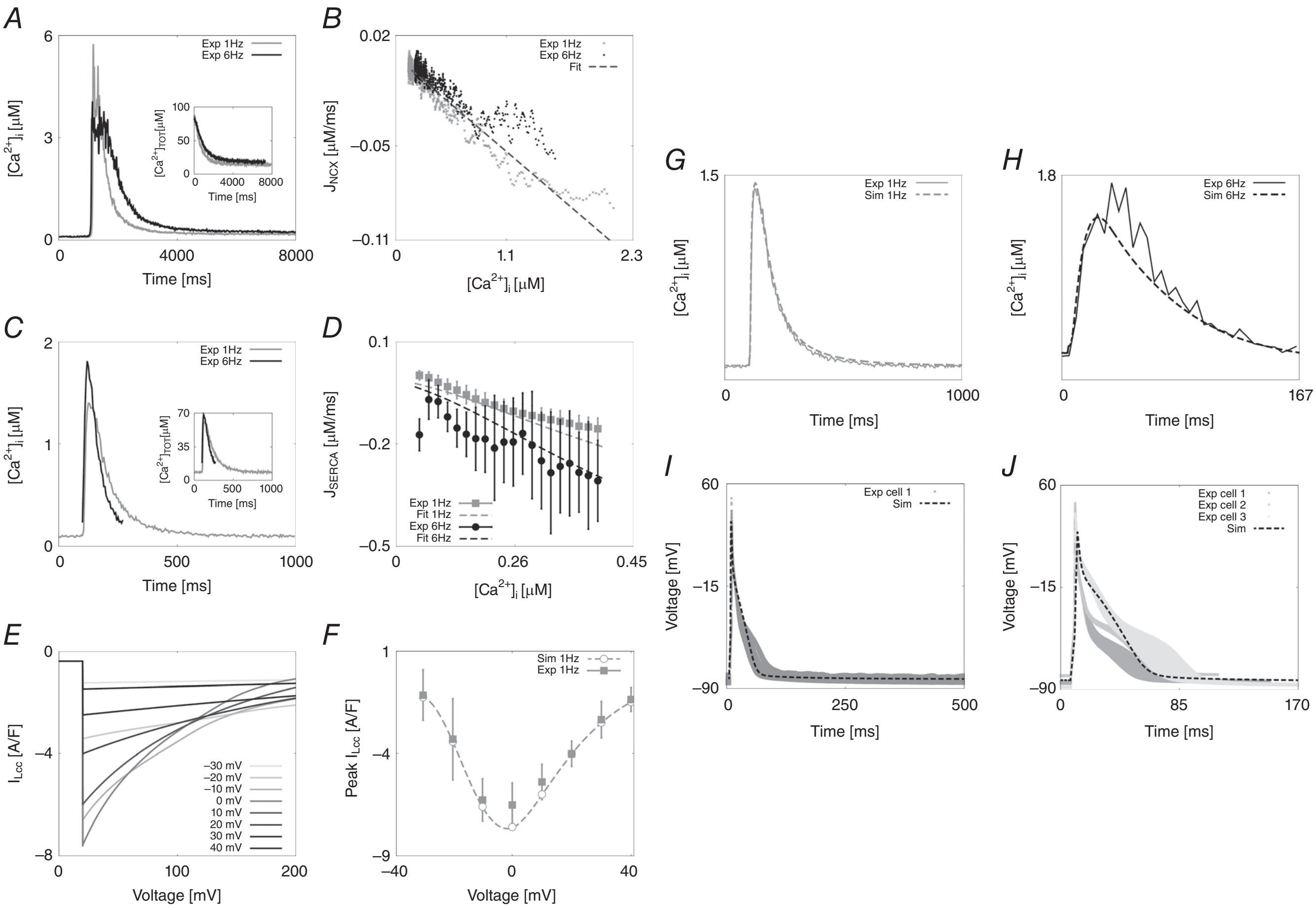

Figure 2. Parameter fitting and model validation
A, NCX fitting procedure. Experimentally measured caffeine-induced transients recorded at 1 Hz (grey) and 6 Hz (black) and correspondent $[\mathrm{Ca}^{2+}]_\mathrm{TOT}$ transient decays used for the fitting (in small window). *B*, NCX fitting results. Comparison of the experimental NCX flux (I_NCX) as a function of internal Ca^{2+} at 1 Hz (grey) and 6 Hz (black) with the line of best fit (dashed black). NCX parameters were fitted in order for the pump to extrude 90% of the measured Ca^{2+} flux during a caffeine transient, while the remaining 10% was used to fit PMCa parameters. *C*, SERCA fitting procedure. Experimentally measured representative Ca^{2+} transients recorded at 1 Hz (grey) and 6 Hz (black) and correspondent $[\mathrm{Ca}^{2+}]_\mathrm{TOT}$ transients (in small window). *D*, SERCA fitting results. Comparison of the experimental SERCA flux (J_SERCA), obtained by integrating the previously fitted models for NCX and PMCa with the Ca^{2+} traces at 1 and 6 Hz and the simulated SERCA flux (dashed lines). To characterize SERCA, the $[\mathrm{Ca}^{2+}]_\mathrm{i}$ fluxes from 157 $[\mathrm{Ca}^{2+}]_\mathrm{i}$ transients measured in 5 cells at 1 Hz and 217 $[\mathrm{Ca}^{2+}]_\mathrm{i}$ transients measured in five different cells at 6 Hz were calculated after 110 ms (at 1 Hz) and 80 ms (at 6 Hz) had elapsed from the peak of the $[\mathrm{Ca}^{2+}]_\mathrm{i}$ transient. The experimentally measured values are expressed by horizontal bars (mean ± σ) with colours representing different frequencies, 1 Hz (grey) and 6 Hz (black). The fittings at 1 and 6 Hz are represented by dashed grey and black lines, respectively, at 1 and 6 Hz. *E*, LCC fitting procedure. Simulated peak current–voltage protocol. A series of voltage clamps are performed between –40 and 40 mV with 10 mV steps, for 200 ms. This simulation allows recording of the dependence of peak L-type current on voltage. *F*, LCC fitting result. Bell-shaped peak I_LCC–V relationship, experiments (squares) and fit (circles and interpolating dashed line). *G*, experimental (continuous grey line) and simulated (dashed grey line) Ca^{2+} transient at 1 Hz. *H*, experimental (continuous black line) and simulated (dashed black line) Ca^{2+} transient at 6 Hz. *I*, experimental (continuous grey line) and simulated (dashed black line) AP at 1 Hz. *J*, experimental (continuous grey lines, for 3 different cells) and simulated (dashed black line) AP at 6 Hz.

Table 1. Experimental and simulated $[Ca^{2+}]_i$ transient characteristics at 1 and 6 Hz

$[Ca^{2+}]$i metrics	Unit	Experimental values	Simulated values
Peak $[Ca^{2+}]$i			
1 Hz	μM	2.000 ± 1.000	1.420
6 Hz	μM	1.900 ± 0.850	1.439
DCa	μM		
1 Hz	μM	0.105 ± 0.016	0.106
6 Hz	μM	0.220 ± 0.090	0.245
RT_{50}			
1 Hz	ms	82 ± 15	111
6 Hz	ms	66 ± 9	61
T_{peak}			
1 Hz	ms	30 ± 9	27
6 Hz	ms	32 ± 8	25

response, decreasing from 1 Hz to 4 or 5 Hz and increasing from 4 or 5 Hz to 6 Hz, depending on $[Ca^{2+}]_o$.

The MCFR in the DD model shows a mild biphasic staircase, negative from 1 Hz to 4 Hz and positive from 4 Hz to 6 Hz at $[Ca^{2+}]_o = 1.8$ mM, with a shift of the turning point to lower frequencies as we decrease $[Ca^{2+}]_o$. Results of the CAMK model and RNaK model show biphasic MCFR, with a shift of the turning point to lower frequencies compared with the DD model at almost all tested levels of $[Ca^{2+}]_o$. The case $[Ca^{2+}]_o = 1.8$ mM in the CAMK model shows positive MCFR. In the NO CAMK model, we report a negative MCFR staircase, at all tested levels of $[Ca^{2+}]_o$.

The DCFR shows a positive staircase with frequency in all the developed models. Compared with the DD model, we see a slight increase in diastolic $[Ca^{2+}]_i$ in the NO CAMK and RNaK models at $[Ca^{2+}]_o = 1.8$ mM.

The $[Ca^{2+}]_{SR}$ frequency response in the DD model is biphasic for $[Ca^{2+}]_o = 1.0$ mM and decreases with frequency for higher tested $[Ca^{2+}]_o$. Biphasic $[Ca^{2+}]_{SR}$ frequency response is also shown in the RNaK model, negative in the range 1 Hz to 2 or 3 Hz and positive in the range 2 or 3 Hz to 6 Hz, depending on $[Ca^{2+}]_o$. A contrasting behaviour is reported in the CAMK and NO CAMK models where the $[Ca^{2+}]_{SR}$ decreases with frequency for almost all tested levels of $[Ca^{2+}]_o$.

When increasing $[Ca^{2+}]_o$, we see a general increase in peak $[Ca^{2+}]_i$ and $[Ca^{2+}]_i$ transient magnitude in all the four models. Interestingly, diastolic $[Ca^{2+}]_i$ shows a decrease at 1–2 Hz followed by an increase at 2–6 Hz.

Intracellular and extracellular fluxes

To observe how single fluxes affect the CFR, we report the changes in all Ca^{2+} fluxes with $[Ca^{2+}]_o$ and frequency. The observed fluxes are the following: sarco/endoplasmic reticulum Ca^{2+}-ATPase (SERCA), ryanodine receptors (RyR), SR leak (SRl), troponin (TRPN), L-type channels (LCC), Na^+/Ca^{2+} exchanger (NCX), sarcolemma Ca^{2+}-ATPase (PMCa) and background Ca^{2+} (CaB). In these reported results, we have included the effect of the rapid calmodulin buffer on the Ca^{2+} fluxes.

Specifically, we have assumed a rapid Ca^{2+} buffering equation for the calmodulin buffer:

$$\frac{d[Ca^{2+}]_i}{dt} = \beta_{CMDN} \cdot \frac{d[Ca^{2+}]_{TOT}}{dt}, \tag{3}$$

where,

$$\beta_{CMDN} = \frac{k_{CMDN} \times B_{CMDN}}{k_{CMDN} + [Ca^{2+}]_i}. \tag{4}$$

Here, k_{CMDN} is the half-saturation constant and B_{CMDN} is the total cytosolic calmodulin concentration, whose values were parameterized from the comprehensive model of the canine ventricular myocyte developed by Greenstein & Winslow (2002), $[Ca^{2+}]_i$ is the intracellular Ca^{2+} concentration and $[Ca^{2+}]_{TOT}$ is the total Ca^{2+} concentration. This means that a portion of the $[Ca^{2+}]_{TOT}$ is buffered and the remaining portion is the free $[Ca^{2+}]_i$.

Equation (1) expands to

$$\frac{d[Ca^{2+}]_i}{dt} = \beta_{CMDN} (I_{LCC} - I_{NCX} - I_{PMCa} + I_{BCa} - I_{SERCA} + I_{RyR} - I_{TRPN} + I_{SRl}), \tag{5}$$

based on

$$\frac{d[Ca^{2+}]_{TOT}}{dt} = \sum Ca^{2+} \text{currents}. \tag{6}$$

Changes in fluxes due to changes in $[Ca^{2+}]_o$ and frequency were observed in two different cases. Inthe first case (without rapid buffering), we integrated and summed the single fluxes to calculate the changes in $[Ca^{2+}]_{TOT}$ with frequency and $[Ca^{2+}]_o$. In the second case (with rapid buffering), we integrated and summed each flux multiplied by the rapid calmodulin buffer coefficient to observe the changes in $[Ca^{2+}]_i$ with frequency and $[Ca^{2+}]_o$. The currents were integrated from the time that the stimulus was applied to the time that the peak calcium transient was reached (T_{peak}). $[Ca^{2+}]_o$ was varied from 1 to 1.8 mM with 0.2 mM steps. Measurements were conducted at steady state and frequency was varied from 1 to 6 Hz with 1 Hz steps. The variation (Δ_I) of the integral (I) as a function of frequency, in the case with and the case without buffering, is presented in Fig. 4. Here, the variation of the integral, for each frequency *i*, is defined as:

$$\Delta_I\ (i) = I\ (i) - \bar{I}, \tag{7}$$

Table 2. Experimental and simulated AP characteristics at 1 and 6 Hz

AP metrics	Units	Experimental values	Simulated values
Resting membrane voltage			
1 Hz	mV	−87.34 ± 1.47	−83.06
6 Hz	mV	−85.16 ± 3.03	−83.16
Peak voltage			
1 Hz	mV	35.26 ± 3.09	38.52
6 Hz	mV	37.43 ± 8.95	28.82
APD_{20}			
1 Hz	ms	1.82 ± 0.27	2.6
6 Hz	ms	1.88 ± 0.62	3.0
APD_{50}			
1 Hz	ms	10.07 ± 1.72	15.7
6 Hz	ms	12.21 ± 6.24	20.6
APD_{70}			
1 Hz	ms	23.09 ± 3.01	33.0
6 Hz	ms	31.01 ± 13.45	34.6
APD_{90}			
1 Hz	ms	43.41 ± 7.08	50.6
6 Hz	ms	55.52 ± 14.51	48.9
Peak dV/dt			
1 Hz	mV	256.84 ± 44.93	171.76
6 Hz	mV	223.16 ± 39.31	132.87

where $\bar{I} = \frac{1}{N}\sum_{i=1}^{N} I(i)$ and N is the number of tested frequencies.

These results identify the main currents responsible for the size and magnitude of the Ca^{2+} transient to be the RYR, SERCA and TRPN Ca^{2+} fluxes. All other currents were one or more orders of magnitude smaller than those. Figure 4 shows the variation of the integrals (Δ_I) up to peak $[Ca^{2+}]_i$ (time $< T_{peak}$) of those currents in the DD model, the total current (TOT) and the sum of the total current plus the diastolic $[Ca^{2+}]_i$ (TOT+DCa), for $[Ca^{2+}]_o = 1.0$, 1.4 and 1.8 mM. To clarify, negative fluxes (SERCA, TRPN) are labelled with (−).

At $[Ca^{2+}]_o = 1.0$ mM, in the case without buffering, the variation of the integral of the total flux up to the peak (TOT) is biphasic. We see an increase in SERCA and a general decrease in TRPN flux, when frequency is increased from 1 to 6 Hz. Here, the biphasic response of the RyR, is responsible for the biphasic PCFR response we have shown in Fig. 3. In fact, in the negative tract of the biphasic PCFR response, the RyR shows a decrease in flux with frequency from 1 to 2 Hz, while in the positive tract of the biphasic PCFR response the RyR shows an increase in flux with frequency from 2 to 6 Hz. These results indicate that the turning point of the RyR efflux, changing from negative to positive staircase with frequency, is consistent with the turning point of the PCFR response. We know that DCa increases with frequency, as reported in many previous studies and demonstrated in the results of our model. Changes in DCa, which are not accounted for in TOT, might thus also play a significant role in PCFR changes. Adding DCa to the total flux (TOT+DCa) we still report the biphasic trend shown in TOT. At $[Ca^{2+}]_o = 1.0$ mM, in the case with buffering, TOT is still biphasic and the biphasic behaviour is further amplified in the TOT+DCa flux.

At $[Ca^{2+}]_o = 1.4$ and 1.8 mM, in the case without buffering, TOT decreases with frequency and adding DCa to the total flux (TOT+DCa) does not change the non-biphasic trend shown for the total flux. Here, the RyR efflux is still biphasic but flattened and the transition from a negative to a positive staircase is shifted to higher frequencies compared with the case at $[Ca^{2+}]_o = 1.0$ mM. In the positive tract of the RyR biphasic response (i.e. at higher frequencies), SERCA activity is enhanced, thus inducing a negative PCFR. The biphasic PCFR at $[Ca^{2+}]_o = 1.4$ and 1.8 mM, seen in Fig. 3, only appears when the effect of the rapid calmodulin buffer is included in the integrals evaluation, revealing the importance of the buffering system in shaping the PCFR response. This result is further amplified by the frequency-dependent increase of DCa, as seen in TOT+DCa. Particularly, in the case $[Ca^{2+}]_o = 1.8$ mM, the DCa induces a shift of the PCFR biphasic turning point to lower frequencies, showing the significant role of DCa in the PCFR.

Discussion

We have developed a biophysical model of rat ventricular cardiac myocyte electrophysiology, parameterized, for the first time to our knowledge, at a physiological temperature and capable of capturing Ca^{2+} and AP responses to changes in pacing frequency. In the baseline DD model, we have reported a biphasic PCFR, shifting from a negative to positive staircase as the rat physiological frequency range is approached, consistent with previously reported studies (Koch-Weser & Blinks, 1963; Borzak *et al.* 1991; Endoh, 2004). Using our modelling framework we have shown that (1) changes in CAMKII-mediated SERCA activity play a major role in shaping the biphasic PCFR; (2) CAMKII-mediated SERCA, LCC and I_{to} activity enhance the biphasic MCFR response; and (3) a reduction of Na^+/K^+ affinity for Na^+ induces a shift of the PCFR and MCFR biphasic staircases. We suggest that the PCFR is mainly driven by the combined effect of the rapid calmodulin buffer and the frequency-dependent changes in DCa.

Model development

The heterogeneity in species and temperature in available measurements able to be used for model parameterization is a notable limitation in the computational physiology approach. This situation hampers model reliability and obfuscates the translation of animal results into human studies. For this reason, the first aim of our work was to develop a species- and temperature-consistent rat electrophysiological model at a physiological frequency and temperature, using consistent experimental data whenever possible. Using the result of this process, our goal was to show the direct link between model parameters and experimental sources.

The main advance of our model is that it significantly reduces the dependency on data from other species and non-physiological temperatures and introduces modified components to reflect temperature effects, as shown in the phylogenetic tree in Fig. 1*C*. In our model, 14 out of 17 components were fitted using rat data and, among those, 13 components were fitted using rat data at physiological temperatures. This compares with 8 out of 16 components parameterized using rat data in previous models.

Our model of the rat ventricular cardiac myocyte electrophysiology matches the experimental measurements that we performed in rat ventricular myocytes at 37°C as seen in 'Results, Comparison between model results and experimental data' and it represents a robust framework to test Ca^{2+} responses to changes in pacing frequency and $[Ca^{2+}]_o$.

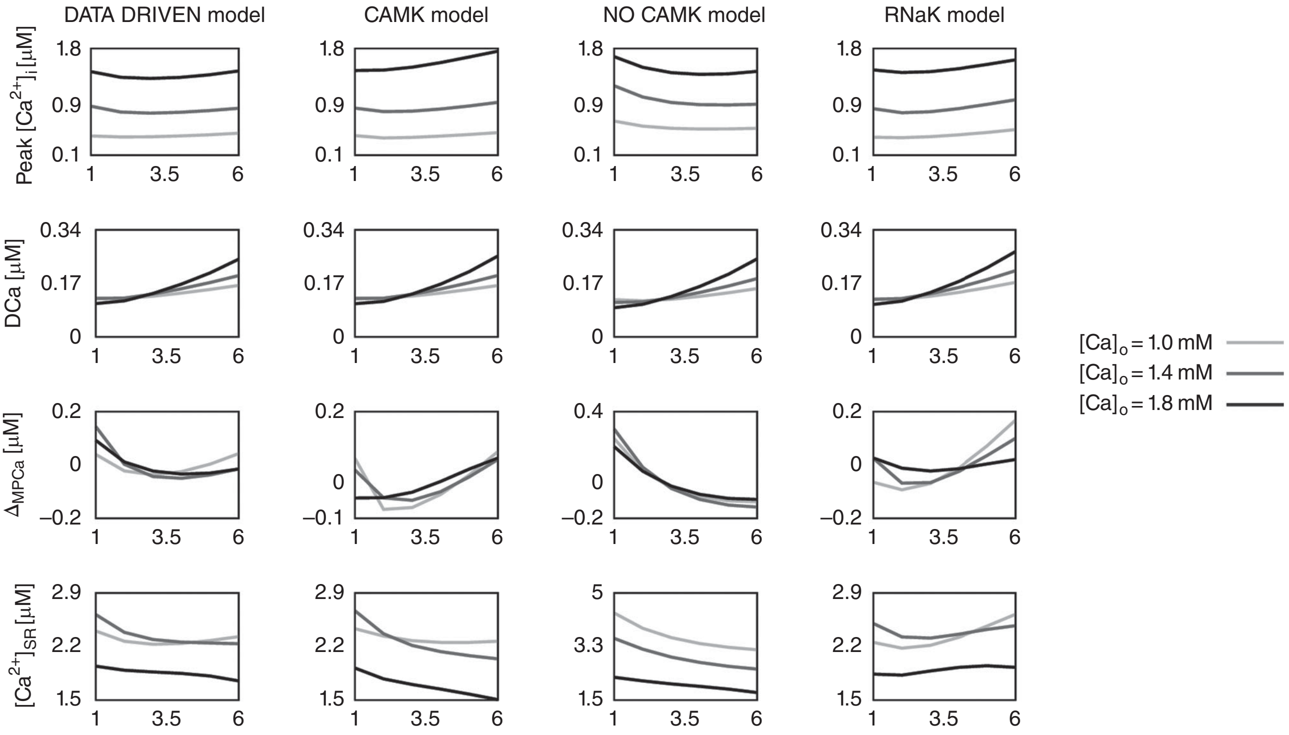

Figure 3. The calcium frequency response (CFR)
Rate-dependent changes in peak $[Ca^{2+}]_i$, diastolic $[Ca^{2+}]_i$ (DCa), magnitude of peak $[Ca^{2+}]_i$ relative variation (Δ_{MPCa}), and Ca^{2+} in the sarcoplasmic reticulum ($[Ca^{2+}]_{SR}$) due to changes in the extracellular Ca^{2+} concentration ($[Ca^{2+}]_o$). Each column represents a different model: the baseline model (DD), a model with inclusion of the CAMKII mediation of LCC and I_{to} activity (CAMK), a model with inhibition of the CAMKII-mediated increase in SERCA activity (NO CAMK) and a model with reduced Na^+/K^+ affinity to Na^+ (RNaK). Different colours represent different $[Ca^{2+}]_o$: 1.0 mM (light grey), 1.4 mM (dark grey) and 1.8 mM (black).

Validation

Using the developed framework, the second aim of our study was to observe the Ca^{2+} response of the model to changes in frequency and $[Ca^{2+}]_o$, as a measure of the FFR.

FFR and CFR measurements are not consistent across the literature. This lack of consensus means that the model cannot match all measurements. Model results at $[Ca^{2+}]_o = 1.8$ mM are, however, consistent with the experimental observations, showing an increase in peak $[Ca^{2+}]_i$ and DCa and a decrease in $[Ca^{2+}]_i$ transient magnitude when increasing frequency from 1 to 6 Hz. It should be noted that while our model was developed at 37°C, changes in temperature have been shown to induce changes in channel behaviour that could also affect the Ca^{2+} response to frequency. Furthermore, we used calibrated measurements, in contrast to the majority of publications in the literature, which only report ratio measurements. If calibrated, ratio measurements would be altered, thus also affecting the observations. To validate our model's predictions, we have compared the simulated PCFR, DCFR and MCFR in our model with experimental data in the literature.

The DD model in Fig. 3 shows a biphasic PCFR, negative in the range 1 Hz to 2 or 3 Hz and positive in the range 2 or 3 Hz to 6 Hz, depending on $[Ca^{2+}]_o$. Borzak *et al.* (1991) showed a biphasic FFR in rats negative in the range 0.1–1 Hz, flat in the range 1–2 Hz and positive in the range 2–6 Hz, which agrees with the biphasic changes in CFR shown in our model. In accordance with our observations, previous work in rats has shown a negative FFR at frequencies lower than 1–2 Hz (Koch-Weser & Blinks, 1963; Capogrossi *et al.* 1986; Mubagwa *et al.* 1997; Layland & Kentish, 1999). The positive PCFR predicted by the model at high frequencies is consistent with the measurements of Dibb *et al.* (2007) and Monasky & Janssen (2009) that show respectively a positive PCFR in rats at 37°C for frequencies in the range 4–8 Hz and a positive PCFR in rats at 37°C when increasing frequency from 4 to 8 Hz at $[Ca^{2+}]_o = 1.5$ mM.

In the DD model, the MCFR shows a biphasic staircase. Our results replicate the MCFR response that we reported in the experimental data at $[Ca^{2+}]_o = 1.8$ mM and are in accordance with Frampton *et al.* (1991) and Picht *et al.* (2007), who showed a negative MCFR respectively in rat for frequencies in the range 0.2–2 Hz and mouse in the range 0.2–4 Hz. Other published works showed a positive MCFR response (Layland & Kentish, 1999; Dibb *et al.* 2007; Monasky & Janssen, 2009). Among those, experiments of Monasky & Janssen (2009) in rats at 37°C showed a positive MCFR increasing frequency from 4 to 8 Hz at $[Ca^{2+}]_o = 1.5$ mM, in accordance with our findings. Layland & Kentish (1999) showed a positive MCFR for

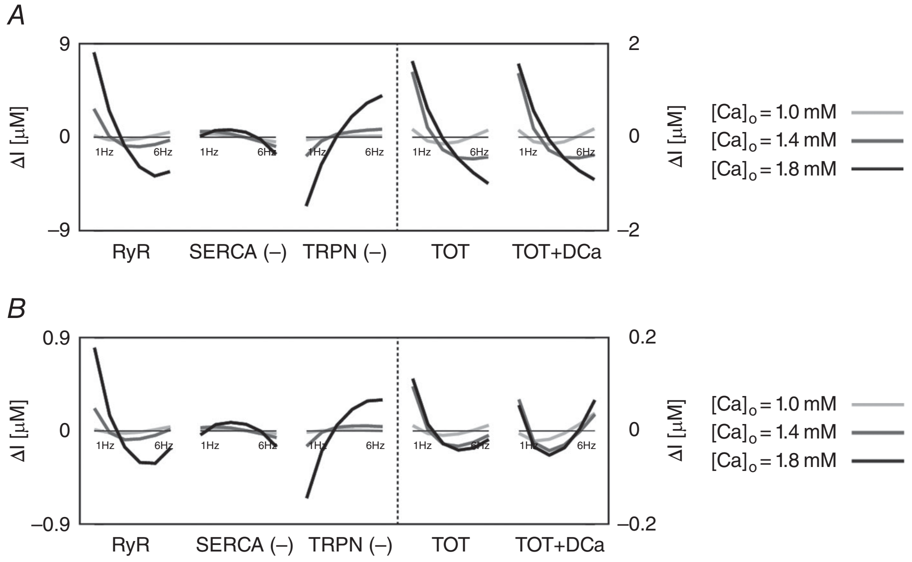

Figure 4. The intracellular and extracellular fluxes behind CFR

DD model intracellular and extracellular current variation of integrals (Δ_{I}) as a function of frequency (1–6 Hz). *A*, DD model without rapid calmodulin buffer. *B*, DD model with rapid calmodulin buffer. In both cases the integrals were evaluated from time = 0 to time = T_{peak}, where T_{peak} is the time to peak of the correspondent simulated Ca^{2+} transient. Colours represent different extracellular Ca^{2+} concentrations: 1 mM (light grey), 1.4 mM (dark grey) and 1.8 mM (black). The most important fluxes, plotted in the figure are the following: ryanodine receptors (RyR), Ca^{2+}-ATPase (SERCA), troponin buffer (TRPN), total current (TOT) and total current plus diastolic Ca^{2+} (TOT+DCa). The other observed fluxes, L-type Ca^{2+} channel (LCC), background Ca^{2+} current (CaB), reverse mode Na^+/Ca^{2+} exchanger (NCXR), forward mode Na^+/Ca^{2+} exchanger (NCXF), Ca^{2+} pump (PMCa) and SR leak current (SRl) were one or more orders of magnitude smaller, and therefore we did not include them in the figure.

all frequencies from 1 to 6 Hz at 30°C and $[\mathrm{Ca}^{2+}]_\mathrm{o}$ = 1.0 mM. Interestingly, when increasing $[\mathrm{Ca}^{2+}]_\mathrm{o}$ to 8 mM, they reported negative PCFR and MCFR in the range 1–2 Hz, thus demonstrating a clear dependency of their observations on the experimental conditions.

DCFR is less often reported and shows a much more consistent behaviour, increasing with frequency in many previous publications (Layland & Kentish, 1999; Dibb *et al.* 2007; Monasky & Janssen, 2009). Consistent with those experiments, our DD model predicts a positive DCFR across frequencies.

Increasing $[\mathrm{Ca}^{2+}]_\mathrm{o}$ caused a general increase in peak $[\mathrm{Ca}^{2+}]_\mathrm{i}$ and $[\mathrm{Ca}^{2+}]_\mathrm{i}$ transient magnitude. This result is consistent with the findings reported by Bouchard & Bose (1989), showing an increase in peak $[\mathrm{Ca}^{2+}]_\mathrm{i}$ in rats, when increasing $[\mathrm{Ca}^{2+}]_\mathrm{o}$ from 0.5 to 2.5 mM. When $[\mathrm{Ca}^{2+}]_\mathrm{o}$ is increased, our model shows a decrease in DCa at 1–2 Hz followed by an increase at 2–6 Hz. Layland & Kentish (1999) reported an increase in DCa with $[\mathrm{Ca}^{2+}]_\mathrm{o}$ at all frequencies, in disagreement with our observations in the range 1–2 Hz. Interestingly, Frampton *et al.* (1991*b*) reported a slight decrease in DCa when increasing $[\mathrm{Ca}^{2+}]_\mathrm{o}$ from 0.5 to 1 mM at 1 Hz frequency in rat measurements at 24°C followed by an increase when further increasing $[\mathrm{Ca}^{2+}]_\mathrm{o}$ to 3 and 6 mM.

The $[\mathrm{Ca}^{2+}]_\mathrm{SR}$ hypothesis and analysis of the intracellular and extracellular fluxes behind CFR

Bers (1989) hypothesised that changes in $[\mathrm{Ca}^{2+}]_\mathrm{SR}$ are responsible for changes in the FFR response, where an increase in $[\mathrm{Ca}^{2+}]_\mathrm{SR}$ induces a positive FFR response and a decrease in $[\mathrm{Ca}^{2+}]_\mathrm{SR}$ induces a negative FFR response. In the DD model at $[\mathrm{Ca}^{2+}]_\mathrm{o}$ = 1.0 mM, the $[\mathrm{Ca}^{2+}]_\mathrm{SR}$ has a biphasic response, negative at lower frequencies and positive at higher frequencies. The $[\mathrm{Ca}^{2+}]_\mathrm{SR}$ decreases with frequency for the remaining tested values of $[\mathrm{Ca}^{2+}]_\mathrm{o}$. These DD model results contradict this hypothesis by showing positive PCFR and negative $[\mathrm{Ca}^{2+}]_\mathrm{SR}$–frequency response.

To observe the role of each of the ion channels on the CFR in the DD model and test how the fast calmodulin buffer affects the response, in Fig. 4 we analysed the variation of the integrals of each one of the Ca^{2+} fluxes in two cases: with and without fast calmodulin buffering. These results showed that the biphasic PCFR response is mainly driven by changes in the RyR flux with frequency at low $[\mathrm{Ca}^{2+}]_\mathrm{o}$ and the effect of the rapid calmodulin buffer at high $[\mathrm{Ca}^{2+}]_\mathrm{o}$. In all cases, changes in RyR efflux modulate the frequency-dependent increase in DCa that, along with the non-linear behaviour of the buffering curve, induces changes in the PCFR.

In Fig. 5, we propose a schematic representation of the mechanism behind changes in the PCFR, due to the DCa and the non-linearity of the buffering curve. Assuming that the DCa_i increases with frequency ($\mathrm{DCa}_\mathrm{i,1Hz} < \mathrm{DCa}_\mathrm{i,6Hz}$), the $\mathrm{DCa}_\mathrm{TOT}$ will increase with frequency ($\mathrm{DCa}_\mathrm{TOT,1Hz} < \mathrm{DCa}_\mathrm{TOT,6Hz}$). The same change in Ca_TOT ($\Delta\mathrm{Ca}_\mathrm{TOT,1Hz} = \Delta\mathrm{Ca}_\mathrm{TOT,6Hz}$), due to the non-linearity of the buffering curve, will translate to a greater change in the Ca_i ($\Delta\mathrm{Ca}_\mathrm{i,1Hz} < \Delta\mathrm{Ca}_\mathrm{i,6Hz}$). In particular, even a smaller change in Ca_TOT ($\Delta\mathrm{Ca}_\mathrm{TOT,6Hz} < \Delta\mathrm{Ca}_\mathrm{TOT,1Hz}$) can result in

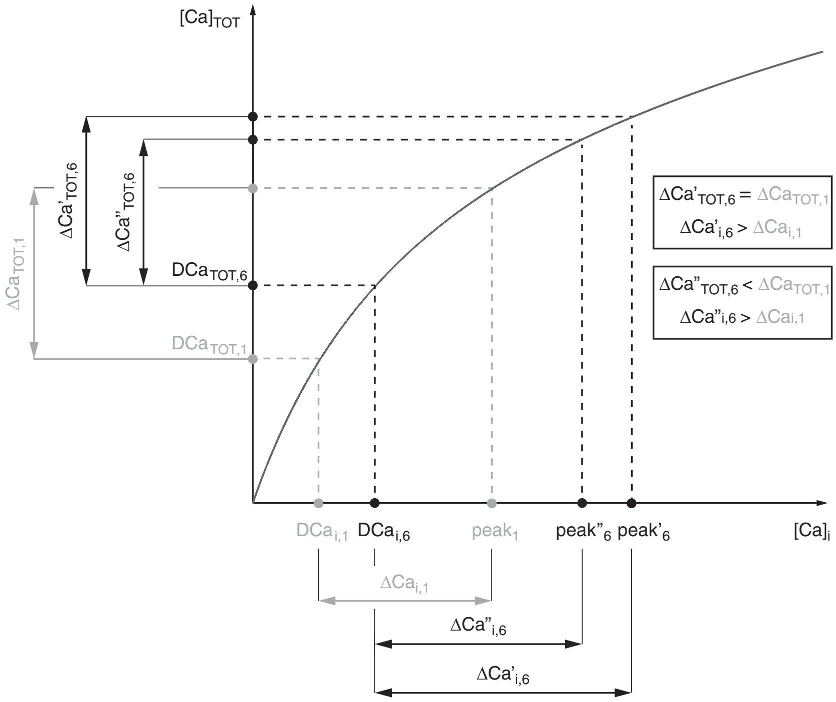

Figure 5. Changes in PCFR due to changes in diastolic calcium and buffering
Schematic diagram showing how changes in diastolic Ca^{2+} (DCa) and a shift of the buffering curve (black curve in figure) affect the PCFR. Assuming that the DCa_i increases with frequency ($\mathrm{DCa}_\mathrm{i,1Hz} < \mathrm{DCa}_\mathrm{i,6Hz}$), the $\mathrm{DCa}_\mathrm{TOT}$ will increase with frequency ($\mathrm{DCa}_\mathrm{TOT,1Hz} < \mathrm{DCa}_\mathrm{TOT,6Hz}$). The same change in Ca_TOT ($\Delta\mathrm{Ca}_\mathrm{TOT,1Hz} = \Delta\mathrm{Ca}_\mathrm{TOT,6Hz}$), due to the non-linearity of the buffering curve, will translate to a greater change in the Ca_i ($\Delta\mathrm{Ca}_\mathrm{i,1Hz} < \Delta\mathrm{Ca}_\mathrm{i,6Hz}$). In particular, even a smaller change in Ca_TOT ($\Delta\mathrm{Ca}_\mathrm{TOT,6Hz} < \Delta\mathrm{Ca}_\mathrm{TOT,1Hz}$) can cause an increase in the Ca_i change ($\Delta\mathrm{Ca}_\mathrm{i,1Hz} < \Delta\mathrm{Ca}_\mathrm{i,6Hz}$). In this way the PCFR response is altered by two distinct mechanisms: the change in DCa and the buffering curve.

increased $\mathrm{Ca_i}$ change ($\Delta\mathrm{Ca}_{\mathrm{i,1Hz}} < \Delta\mathrm{Ca}_{\mathrm{i,6Hz}}$). In this way the PCFR response is altered by two distinct mechanisms: the change in DCa with frequency and the buffering curve. The effects of the buffering curve on the PCFR were shown to be particularly prominent with increasing $[\mathrm{Ca}^{2+}]_\mathrm{o}$. As we have reported in our results, increased $[\mathrm{Ca}^{2+}]_\mathrm{o}$ translates to increased $[\mathrm{Ca}^{2+}]_\mathrm{i}$, which, in turn, causes a shift towards a shallower area of the buffering curve, where this mechanism is more accentuated.

Overall, these results show that the biphasic PCFR is caused by the biphasic staircase of the RyR efflux at $[\mathrm{Ca}^{2+}]_\mathrm{o} = 1.0$ mM. However, the flattened biphasic behaviour of the RyR release is balanced by the increase of SERCA activity with frequency and is not sufficient to generate a biphasic PCFR response at $[\mathrm{Ca}^{2+}]_\mathrm{o} = 1.4$ and 1.8 mM. In our analysis, the biphasic PCFR response is caused by the non-linearity of the buffering curve. The RyRs and SERCA operate by modulating DCa, which further amplifies the behaviour. Notably, this mechanism is model independent, as both the increase in DCa with frequency and the non-linearity of the buffering curve are well-known properties of ventricular myocytes. The mechanism behind PCFR changes, shown in Fig. 5, explains how the buffering system and DCa affect the PCFR response.

Model variants still reveal the importance of the buffering system on the PCFR

As already discussed, previous works in rats proposed the hypotheses that CAMKII regulation of the L-type channel, I_{to} current and SERCA activity and a reduction of the $\mathrm{Na^+/K^+}$ pump affinity to $\mathrm{Na^+}$ could be responsible for alterations in the FFR and CFR responses. In our work we tested these hypotheses by altering the DD model to simulate those conditions.

Results of the CAMK model in Fig. 3 show that the PCFR is qualitatively the same as that of the DD model, although we report a positive PCFR at $[\mathrm{Ca}^{2+}]_\mathrm{o} = 1.8$ mM and a clear enhancement of the MCFR positive staircase. Additional simulations revealed the same mechanism already presented for the DD model in the previous section ('Discussion, The $[\mathrm{Ca}^{2+}]_{\mathrm{SR}}$ hypothesis and analysis of the intracellular and extracellular fluxes behind CFR'), showing that the PCFR is mainly driven by the RyR flux, with a clear effect of the rapid calmodulin buffer and DCa on the response, especially at high levels of $[\mathrm{Ca}^{2+}]_\mathrm{o}$ (for further details see section 6.1 of Appendix). Interestingly, previous studies showed positive MCFR response (Layland & Kentish, 1999; Dibb *et al.* 2007; Monasky & Janssen, 2009) that was not replicated in our DD model but is significantly enhanced in the CAMK model, highlighting the importance of CAMKII regulation on the MCFR. These results show that CAMKII-mediated activity, directly acting on Ca^{2+} release from the RyR, enhances the positive MCFR staircase.

Analysis of the NO CAMK model reveals that CAMK inhibition mainly affects the PCFR, MCFR and $[\mathrm{Ca}^{2+}]_{\mathrm{SR}}$. Compared with the biphasic behaviour in the DD model, the NO CAMK model in Fig. 3 reveals a flattened PCFR staircase, negative MCFR in all cases and a notable increase in $[\mathrm{Ca}^{2+}]_{\mathrm{SR}}$ at low frequencies compared with the DD model, which in turn activates more Ca^{2+} release from the RyR. Consistent with our results of the DD model, additional simulations showed that the RyR flux and the dependent increase in DCa are the main responsible for the PCFR staircase in this case (for further details see section 6.2 of Appendix). Our results are consistent with Wu *et al.* (2012) who showed that CAMKII inhibition flattens the FFR response in mice. These results show that CAMKII up-regulated SERCA modulates the shift from negative to positive PCFR by altering the $[\mathrm{Ca}^{2+}]_{\mathrm{SR}}$, inducing changes in the RyR frequency response.

Compared with the DD model, results of the RNaK model in Fig. 3 show a shift of the turning point of the biphasic PCFR and MCFR responses to lower frequencies, reduced $[\mathrm{Na}^+]_\mathrm{i}$ for frequencies < 2 or 3 Hz and augmented $[\mathrm{Na}^+]_\mathrm{i}$ for frequencies > 2 or 3 Hz depending on $[\mathrm{Ca}^{2+}]_\mathrm{o}$. The biphasic PCFR response here reveals the same mechanism as demonstrated in the DD model (for further details see section 6.3 of Appendix). Decreasing the $\mathrm{Na^+/K^+}$ pump affinity for $\mathrm{Na^+}$, our model shows positive PCFR and MCFR for frequencies > 2 or 3 Hz depending on $[\mathrm{Ca}^{2+}]_\mathrm{o}$, highlighting the role of $[\mathrm{Na}^+]_\mathrm{i}$ in enhancing the positive staircase effect at physiological frequencies, as suggested by Langer *et al.* (1975).

Conclusions

In our work, we have concluded that a biphasic PCFR response in rats at 37°C is due to the biphasic behaviour of the RyR efflux at low $[\mathrm{Ca}^{2+}]_\mathrm{o}$ and the combined effect of the Ca^{2+} buffering mechanism and the frequency-dependent increase in DCa at higher levels of $[\mathrm{Ca}^{2+}]_\mathrm{o}$. This result is consistent with the observation of a shift from negative to positive FFR when approaching the rat physiological range of frequencies. We have shown that CAMKII-mediated SERCA, LCC and I_{to} activity, directly acting on Ca^{2+} release from the RyR, enhances the positive MCFR staircase. Absence of a CAMKII-mediated increase in SERCA activity affects the CFR by altering the $[\mathrm{Ca}^{2+}]_{\mathrm{SR}}$ frequency response, which in turn affects RyR release, flattening the PCFR and inducing negative MCFR. Reduced $\mathrm{Na^+/K^+}$ affinity to $\mathrm{Na^+}$ acts on the CFR, increasing $[\mathrm{Na}^+]_\mathrm{i}$ and $[\mathrm{Ca}^{2+}]_\mathrm{i}$ at high frequencies and inducing a shift of the biphasic PCFR and MCFR turning point to lower frequencies.

Appendix: Development of the DD model, the parameter fitting procedure and further information about model's alterations and limitations

To achieve a model that captures rat cardiac electrophysiology and can simulate graded response, we combined the Pandit electrophysiology framework (Pandit *et al.* 2001) with the Hinch calcium dynamics model (Hinch *et al.* 2004). Figure 6 shows the components taken from the Pandit model (in black) and the Hinch model (in grey). Section 1 describes the model development and parameter refitting procedure. In this section we show how we developed the reconciliation of units between the two models, we describe choices for cell, SR volume and capacitance parameters, intracellular and extracellular Na$^+$ and K$^+$ concentrations, fixed ionic concentrations and buffers, and we describe the parameter fitting procedure for all the fitted channels within the model. Section 2 describes the results for all simulated Ca^{2+} and AP phenotypes at frequencies from 1 to 6 Hz with step 1 Hz. In sections 3 and 4 we show the effects of changes in $[\mathrm{K}^+]_\mathrm{o}$ and AP on the PCFR, DCFR, MCFR and $[\mathrm{Ca}^{2+}]_\mathrm{SR}$ frequency response. Section 5 describes how we included CAMKII alteration of L-type channel and transient outward K$^+$ current in the CAMK model. Sections 6 and 7 provide insight about the differences in CFR in the CAMK, NO CAMK and RNaK model compared with the DD model.

Model development and parameter refitting

We explain in detail the coupling between the Pandit (Pandit *et al.* 2001) and Hinch (Hinch *et al.* 2004) models and the parameter fitting procedure that we adopted to reparametrize the developed electrophysiology framework.

Model development

Unit and structural consistency. The movement of ions across the cell membrane can be represented in terms of ion fluxes or whole-cell current. In the Hinch model all the ionic transports are expressed in terms of calcium ions flux in millimolar per millisecond whereas in the Pandit model all the cell currents are represented in nanoamps. This type of inconsistency cannot be simply solved using an automated conversion between equivalent units but instead requires additional information regarding the volume of the myocyte or the valence of the species. Using the same approach developed by Terkildsen *et al.* (2008), we converted the Hinch calcium fluxes into compatible calcium currents using the formula:

$$I_{\mathrm{New}} = jzFV_{\mathrm{myo}}, \tag{A1}$$

where j is the flux (in Hinch), z is the valence, F is the Faraday constant and V_{myo} is the volume of the myocyte (see Table 3).

In general, units are expressed in ms, mV, mM, μA, μF, mS.

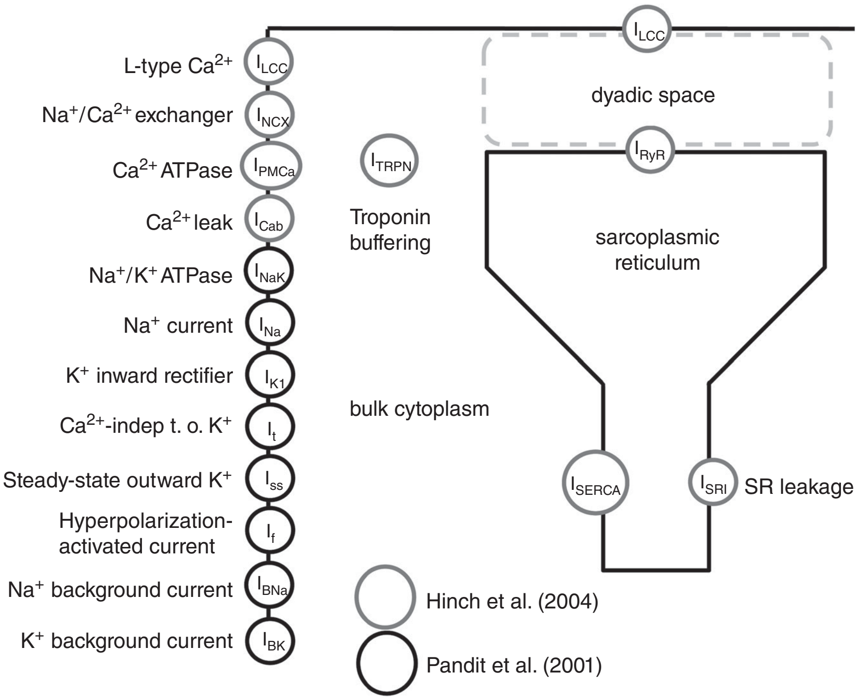

Figure 6. Inheritance of components in our model
Schematic showing the coupling between Pandit and Hinch models. Components are highlighted in black when their equations were kept from Pandit, in grey when their equations were kept from Hinch.

Table 3. Capacitance and volumes

Parameter	Unit	Definition
$C_M = 0.0001$	μF	Membrane capacitance
$V_{myo} = 25,850$	μm^3	Volume of the myocyte
$V_{myo_{uL}} = 2.585 \times 10^{-5}$	μL	Volume of the myocyte
$V_{SR_{uL}} = 2.098 \times 10^{-6}$	μL	Volume of the SR

Cell, SR volume and capacitance. The membrane capacitance C_m was kept from the original Pandit model, based on experimental measurements in rat ventricular cells (Clark *et al.* 1993). The cell and SR volumes were maintained from Hinch *et al.* (2004), based on Greenstein & Winslow (2002) (see Table 3).

Na^+ and intracellular and extracellular concentrations. We assumed $[Na^+]_i = 10$ mM at 1 Hz, consistent with experiments developed in rats at 37°C (Harrison *et al.* 1992). Following the hypothesis by which increase in rate might produce increase in intracellular sodium ($[Na^+]_i$) (Woodbury, 1963; Cohen *et al.* 1982; Maier *et al.* 1997), we assumed $[Na^+]_i = 14$ mM at 6 Hz. Extracellular sodium ($[Na^+]_o$) was held fixed to a value of $[Na^+]_o = 140$ mM following experiments conducted in rats. Extracellular potassium ($[K^+]_o$) was set to a value of $[K^+]_o = 5.4$ mM at all frequencies. Experimentally measured intracellular and extracellular Na^+ concentrations in previous works can be observed in Table 4 while intracellular and extracellular concentrations in previous works can be observed in Table 5.

Fixed ionic concentrations and buffers. The Ca^{2+}-binding proteins included in our model are troponin, calmodulin and EGTA. Total cytosolic calmodulin concentration (B_{CMDN}) and half-saturation constant (K_{CMDN}) values were taken from the comprehensive model of canine ventricular myocyte developed by Greenstein & Winslow (2002). Ca^{2+} buffering to TRPN was modelled as described by Hinch *et al.* (2004). All troponin parameters were obtained from the model of ferret ventricular myocytes at room temperature (Bondarenko *et al.* 2004). The effects of the intracellular Ca^{2+} buffer EGTA were also modelled as described by Pandit, following an adaptation from (Winslow *et al.* 1999) mimicking the experimental conditions developed in Shimoni *et al.* (1995). The Ca^{2+}-binding protein parameters are shown in Table 6.

Parameter refitting procedure

Membrane Ca^{2+} extrusion: Na^+/Ca^+ exchanger (I_{NCX}) and Ca^{2+} pump (I_{PMCa}). In single cell experiments, caffeine triggers full release of $[Ca^{2+}]_{SR}$, with subsequent increase of $[Ca^{2+}]_i$ (Blayney *et al.* 1978; Klein *et al.* 1990; Sitsapesan & Williams, 1990; Meissner *et al.* 1997; Herrmann-Frank *et al.* 1999). There are three main mechanisms of Ca^{2+} extrusion from the cytosol: I_{NCX}, I_{PMCa} and I_{SERCA}. The presence of caffeine assures inhibition of the SERCA pump, which is no longer able to drive Ca^{2+} back to the SR allowing the assumption, exploited for the purposes of model fitting, that no Ca^{2+} SR reuptake occurs. This leaves only two currents actively contributing to Ca^{2+} extrusion: I_{NCX} and I_{PMCa}. During caffeine-induced transients in rats, NCX and PMCa account for approximately 80–90% and 10–20% of the Ca^{2+} extrusion from the cell, respectively (Bassani *et al.* 1992; Choi & Eisner, 1999; Bers, 2001).

In our work, the experimental caffeine-induced Ca^{2+} transients at 1 and 6 Hz were converted to the total cytosolic Ca^{2+} concentration ($[Ca^{2+}]_{TOT}$)using the following fast buffering approximation proposed by Trafford *et al.* (1999):

$$[Ca^{2+}]_{TOT} = [Ca^{2+}]_i + [Ca^{2+}]_{buffered} = [Ca^{2+}]_i + \sum B_{buffer} \frac{[Ca^{2+}]_i}{([Ca^{2+}]_i + K_{buffer})}, \qquad \text{(A2)}$$

where K_{buffer} is the affinity of the buffer and B_{buffer} is its concentration (the buffers used in our model are troponin, calmodulin and EGTA). This type of conversion is necessary because the calibrated fluorescence measurements describe the change in intracellular free Ca^{2+} ($[Ca^{2+}]_i$) and for our fitting purposes we are interested in the total flux of Ca^{2+} ions across the membrane ($[Ca^{2+}]_{TOT}$). After defining Peak$[Ca^{2+}]_{TOT}$ as the maximum value of $[Ca^{2+}]_{TOT}$, each converted caffeine transient was separated into an early release phase, which occurred prior to Peak$[Ca^{2+}]_{TOT}$, and a later exponential decay, occurring after Peak$[Ca^{2+}]_{TOT}$, where the membrane calcium transporters extrude Ca^{2+} from the cytosol. The change in total amount of Ca^{2+} over time can be described as a differential equation:

$$\frac{d[Ca^{2+}]_{TOT}}{dt} \cong J_{IN} - J_{OUT}, \qquad \text{(A3)}$$

where $J_{IN} = J_{LCC} + J_{RYR}$ and $J_{OUT} = J_{SERCA} + J_{NCX} + J_{PMCa}$. Focusing on the later exponential decay of the caffeine-induced $[Ca^{2+}]_{TOT}$ transient and assuming that only I_{PMCa} and I_{NCX} are active, this reduces to:

$$\frac{d[Ca^{2+}]_{TOT}}{dt} \cong -J_{NCX} - J_{PMCa}. \qquad \text{(A4)}$$

For this reason, we fitted the Ca^{2+}-dependent kinetics of the remaining two transporters to the later exponential decay of the curve. We assumed that the contribution of I_{PMCa} to the decay is comparatively small and we attributed 90% of the total Ca^{2+} extrusion to I_{NCX}. The flux through the NCX exchanger was modelled using the formulation

Table 4. Na^+ Intracellular and extracellular concentrations
NR: not reported

Publication	Temperature (°C)	Frequency (Hz)	$[Na^+]_i$ (mM)	$[Na^+]_o$ (mM)
Polimeni (1974)	NR	NR	21 ± 1	140 ± 2
Polimeni & Al-Sadir (1975)	NR	NR	NR	134 ± 1
Shattock & Bers (1989)	30	1	16.71 ± 0.6	NR
Harrison *et al*. (1992)	37	1	10.26 ± 0.23	NR
Borzak *et al*. (1992)	37	NR	14 ± 2	NR
Donoso *et al*. (1992)	27	1	10.7 ± 1.2	NR
Levi *et al*. (1994)	30	1	10.9 ± 0.74	NR
Baartscheer *et al*. (1997)	37	8	9.6 ± 0.4	NR
Despa *et al*. (2002)	25	Rest	11.1 ± 0.7	NR

Table 5. K^+ intracellular and extracellular concentrations
NR: not reported

Publication	Temperature (°C)	Frequency (Hz)	$[K^+]_i$ (mM)	$[K^+]_o$ (mM)
Page & Page (1968)	22–24	NR	151	NR
Polimeni (1974)	NR	NR	151 ± 2	3.6 ± 0.1
Polimeni & Al-Sadir (1975)	NR	NR	NR	4.6 ± 0.2
Powell (1980)	37	NR	120.8 ± 1.7	NR

Table 6. Fixed ionic concentrations and buffers

Parameter	Unit	Definition
$B_{\mathrm{CMDN}} = 0.05$	mM	Total cytosolic calmodulin concentration
$K_{\mathrm{CMDN}} = 2.382 \times 10^{-3}$	mM	Half-saturation constant of calmodulin
$K\mathrm{trpn}_{+} = 0.04 \times 10^{3}$	$\mathrm{mM^{-1}\ ms^{-1}}$	Binding rate of calcium to troponin
$K\mathrm{trpn}_{-} = 0.04$	$\mathrm{ms^{-1}}$	Dissociation rate of calcium to troponin
$K\mathrm{m}_{\mathrm{EGTA}} = 1.5 \times 10^{-4}$	mM	Calcium half-saturation constant for EGTA

from Hinch *et al.* (2004), developed by Luo & Rudy (1994):

$$J_{\mathrm{NCX}} = \frac{g_{\mathrm{NCX}}\left(e^{\eta\frac{FV}{RT}}[\mathrm{Na}^+]_i^3[\mathrm{Ca}^{2+}]_o - e^{(\eta-1)\frac{FV}{RT}}[\mathrm{Na}^+]_o^3[\mathrm{Ca}^{2+}]_i\right)}{\left(K_{\mathrm{mNa}}^3 + [\mathrm{Na}^+]_o^3\right)\left(K_{\mathrm{mNa}} + [\mathrm{Ca}^{2+}]_o\right) + \left(1 + K_{\mathrm{sat}}e^{(\eta-1)\frac{FV}{RT}}\right)}, \tag{A5}$$

where g_{NCX} is the pump rate of NCX, η is the parameter describing the dependence of NCX flux on voltage, F is the Faraday constant, V is voltage, R is the universal gas constant, T is temperature, K_{mNa} is the Na^+ half-saturation of NCX, K_{mCa} is the Ca^{2+} half-saturation of NCX, K_{sat} is the low potential saturation factor of NCX and $[\mathrm{Na}^+]_i$, $[\mathrm{Ca}^{2+}]_i$, $[\mathrm{Na}^+]_o$ and $[\mathrm{Ca}^{2+}]_o$ are the intracellular and extracellular Na^+ and Ca^{2+} concentrations, respectively. All the parameters involved in the NCX formulation, except for g_{NCX}, where kept from Hinch *et al.* (2004). Because $[\mathrm{Na}^+]_i$ is unlikely to change during the period that NCX is active, $[\mathrm{Na}^+]_i$ was assumed constant for the fitting, with a value $[\mathrm{Na}^+]_i = 10$ mM. This implies that the equation takes the form of a first-degree polynomial having two parameters: $J_{\mathrm{NCX}} = a[\mathrm{Ca}^{2+}]_i + b$. As no major changes in NCX behaviour at different frequencies are reported in the literature, we fitted a linear relation along the two data sets at 1 and 6 Hz and evaluated the conductivity of the exchanger to be $g_{\mathrm{NCX}} = 0.0515\ \mathrm{mM\ ms^{-1}}$.

Current through the Ca^{2+} pump was modelled using the formulation from Hinch *et al.* (2004), first published in Luo & Rudy (1994):

$$I_{\mathrm{PMCa}} = \frac{g_{\mathrm{PMCa}}[\mathrm{Ca}^{2+}]_i}{K_{\mathrm{PMCa}} + [\mathrm{Ca}^{2+}]_i}, \tag{A6}$$

where g_{PMCa} is the maximal pump rate and K_{PMCa} is the half-saturation rate. In our simulations, I_{PMCa} makes approximately 10% of the NCX job at both 1 and 6 Hz frequencies, which agrees with the reported percentage in the literature (Bers, 2001). Therefore, there was no need to re-parameterize the pump. Parameter values were maintained from the Hinch model (Hinch *et al.* 2004): $g_{\mathrm{PMCa}} = 5 \times 10^{-6}$ mM ms^{-1} and $K_{\mathrm{PMCa}} = 0.00035$ mM.

Sarco/endoplasmic reticulum Ca^{2+}-ATPase (SERCA). We assumed that during a field stimulated Ca^{2+} transient there are two sources of $[\mathrm{Ca}^{2+}]_{\mathrm{i}}$ (I_{LCC} and I_{RYR}) and three $[\mathrm{Ca}^{2+}]_{\mathrm{i}}$ sinks currents (I_{NCX}, I_{PMCa} and I_{SERCA}). Fluorescence experiments in rats, performed under whole-cell voltage-clamp conditions and in the presence of EGTA to detect Ca^{2+} sparks (Song *et al.* 1998), revealed that after 80–100 ms, both I_{LCC} and I_{RYR} Ca^{2+} pathways are closed and the cell predominantly extrudes Ca^{2+} from the cytosol through I_{NCX}, I_{PMCa} and I_{SERCA}. This implies that the effects of $[\mathrm{Ca}^{2+}]_{\mathrm{i}}$ influx through I_{LCC} and $[\mathrm{Ca}^{2+}]_{\mathrm{i}}$ release through I_{RYR} can be neglected when analysing the later part of the $[\mathrm{Ca}^{2+}]_{\mathrm{i}}$ transient. Furthermore, using the models of I_{NCX} and I_{PMCa} described above, we can remove their effects on the change in Ca^{2+} to isolate the extrusion of Ca^{2+} attributed to SERCA. It must be noted that at higher pacing the pump's uptake becomes faster to facilitate frequency-dependent acceleration of relaxation, a process mediated by Ca^{2+}/calmodulin kinase II (CaMKII) that still remains unclear (Li *et al.* 1998; Hagemann *et al.* 2000; Huke & Bers, 2007).

In our work, the experimentally recorded Ca^{2+} transients were first converted to the total cytosolic Ca^{2+} concentration $[\mathrm{Ca}^{2+}]_{\mathrm{TOT}}$ (see eqn (A2)) and then used for fitting purposes. The behaviour of the pump was studied taking into account the decay phase of the $[\mathrm{Ca}^{2+}]_{\mathrm{i}}$ transients elicited by field stimulation at 1 and 6 Hz, integrated with the previously fitted models for I_{NCX} and I_{PMCa}. To characterize SERCA, the $[\mathrm{Ca}^{2+}]_{\mathrm{i}}$ fluxes from 157 $[\mathrm{Ca}^{2+}]_{\mathrm{i}}$ transients measured in five cells at 1 Hz and 217 $[\mathrm{Ca}^{2+}]_{\mathrm{i}}$ transients measured in five different cells at 6 Hz were calculated after 110 ms (at 1 Hz) and 80 ms (at 6 Hz) had elapsed from the peak of the $[\mathrm{Ca}^{2+}]_{\mathrm{i}}$ transient. The flux through SERCA (I_{SERCA}) was modelled using the formulation from Hinch *et al.* (2004), previously published in Jafri *et al.* (1998):

$$I_{\mathrm{SERCA}} = g_{\mathrm{SERCA}} \frac{[\mathrm{Ca}^{2+}]_{\mathrm{i}}^{2}}{K_{\mathrm{SERCA}}^{2} + [\mathrm{Ca}^{2+}]_{\mathrm{i}}^{2}}, \qquad \text{(A7)}$$

where g_{SERCA} and K_{SERCA} are the maximum pump rate and the half-saturation of the SERCA pump, respectively. Plotting the change in total flux of Ca^{2+} across the membrane in time ($\mathrm{d}[\mathrm{Ca}^{2+}]_{\mathrm{TOT}}/\mathrm{d}t$) against the $[\mathrm{Ca}^{2+}]_{\mathrm{free}}$ we fitted the function $y = a\frac{x^2}{b^2+x^2}$ through our data and we evaluated the parameters a and b, respectively representing g_{SERCA} and K_{SERCA}. The SERCA formulation within the Hinch model (Hinch *et al.* 2004) did not take into account the frequency-dependent behaviour. To approximate the lack of calmodulin up-regulation of SERCA at different electrophysiological frequencies, we fitted the conductivity of the pump at 1 Hz ($g_{\mathrm{SERCA1}} = 0.47 \times 10^{-3}$ μM^3 ms^{-1}) and 6 Hz ($g_{\mathrm{SERCA6}} = 0.68 \times 10^{-3}$ μM^3 ms^{-1}) by assuming that the affinity parameter ($K_{\mathrm{SERCA}} = 0.45 \times 10^{-3}$ mM) did not change with frequency, consistent with the findings previously reported in the literature (Picht *et al.* 2007). Following the approach already used by Li *et al.* (2010), we included a CaMKII regulation model in the developed framework to simulate the effects of pacing frequency. The model, proposed by Hund and Rudy for canine ventricular myocytes (Hund & Rudy, 2004) and adapted from more recent finding by Li *et al.* (2010), includes three states representing the fractional occupancies of active CaMKII (f_{a}), bound CaMKII (f_{b}) and trapped CaMKII (f_{t}):

$$\frac{\mathrm{d}f_t}{\mathrm{d}t} = \alpha f_{\mathrm{b}}(f_{\mathrm{b}} + f_{\mathrm{t}}) - \beta f_{\mathrm{t}}, \qquad \text{(A8)}$$

$$f_{\mathrm{b}} = f_0(1 - f_{\mathrm{t}}) \cdot \frac{1}{1 + \frac{K_{\mathrm{mCaM}}}{[\mathrm{Ca}^{2+}]_{\mathrm{i}}}}, \qquad \text{(A9)}$$

$$f_{\mathrm{a}} = f_{\mathrm{b}} + f_{\mathrm{t}}, \qquad \text{(A10)}$$

where α (0.05 ms$^{-2)}$ and β (0.0002 ms^{-1}) are the phosphorylation and dephosphorylation rates of CaMKII, respectively, f_0 (5%) is the fraction of active CaMKII binding sites at equilibrium and K_{mCaM} (0.7 μM) is the $[\mathrm{Ca}^{2+}]_{\mathrm{i}}$ concentration at half-maximum CaMKII activation. Using the experimental representative Ca^{2+} transients at 1 and 6 Hz, we measured the level of active CaMKII at both frequencies and we modelled the dependence of I_{SERCA} on the kinase by defining g_{SERCA} and K_{SERCA} as a function of f_{a}:

$$I_{\mathrm{SERCA}} = g_{\mathrm{SERCA}} \cdot \frac{[\mathrm{Ca}^{2+}]_{\mathrm{i}}^{2}}{K_{\mathrm{SERCA}}^{2} + [\mathrm{Ca}^{2+}]_{\mathrm{i}}^{2}}, \qquad \text{(A11)}$$

$$g_{\mathrm{SERCA}} = \overline{\Delta_{g_{\mathrm{CaMK}}}} \cdot \frac{f_{\mathrm{a}}}{K_{\mathrm{m,CaMK}} - f_{\mathrm{a}}}, \qquad \text{(A12)}$$

where Δ_{gCaMK} is the maximum increase in g_{SERCA} due to CaMKII and $K_{\mathrm{m,CaMK}}$ is the half-saturation coefficients. The line of best fit for $\underline{g_{\mathrm{SERCA}}}$ plotted against f_{a} resulted in $K_{\mathrm{m,CaMK}} = 2.224$ and $\overline{\Delta_{g_{\mathrm{CaMK}}}} = 0.001158$.

L-type Ca^{2+} channels (LCCs) and Ryanodine Receptors (RyR). The function of the LCC was investigated using the experimentally recorded peak I_{LCC}–V relationship curve. During the peak I_{LCC}–V experiment the membrane potential is held fixed at −40 mV and then clamped between −40 mV and 40 mV with 10 mV steps (see Fig. 2*E* and *F*). I_{Na} contribution is negligible, since the holding potential around −40 mV assures inactivation of the Na^{+} channel and the K^{+} currents are pharmacologically blocked. The peak transmembrane current is recorded at each membrane potential and gives an approximation of the I_{LCC} current.

In our work, the current through the L-type channels was modelled using the formulation from Hinch *et al.* (2004), a simplified Markovian model of the Jafri *et al.* (1998) model. The I_{LCC} representation presents three states, I (inactivated), C (closed) and O (open), with the respective probabilities to move from one state to another:

$$\alpha_{+} = \frac{e^{\frac{(V-V_{\mathrm{L}})}{\Delta V_{\mathrm{L}}}}}{t_{\mathrm{L}}\left(e^{\frac{(V-V_{\mathrm{L}})}{\Delta V_{\mathrm{L}}}}+1\right)}, \tag{A13}$$

$$\alpha_{-} = \frac{\phi_{\mathrm{L}}}{t_{\mathrm{L}}}, \tag{A14}$$

$$\epsilon_{+}\left([\mathrm{Ca}^{2+}]_{\mathrm{ds}}\right) = \frac{[\mathrm{Ca}^{2+}]_{\mathrm{ds}}\left(e^{\frac{(V-V_{\mathrm{L}})}{\Delta V_{\mathrm{L}}}}+a\right)}{\tau_{\mathrm{L}}K_{\mathrm{L}}\left(e^{\frac{(V-V_{\mathrm{L}})}{\Delta V_{\mathrm{L}}}}+1\right)}, \tag{A15}$$

$$\epsilon_{-} = \frac{b\left(e^{\frac{(V-V_{\mathrm{L}})}{\Delta V_{\mathrm{L}}}}+a\right)}{\tau_{\mathrm{L}}\left(be^{\frac{(V-V_{\mathrm{L}})}{\Delta V_{\mathrm{L}}}}+a\right)}, \tag{A16}$$

where V_{L} is the potential when 50% of the LCCs channels are open, Δ_{VL} is the width of opening potentials, φ_{L} is the proportion of time the channels are still closed but in open mode, t_{L} is the time switching between closed and open states, T_{L} is the inactivation time, K_{L} is the concentration when the LCCs inactivate, a and b are the biasings to make inactivation a function of V and J_{L} is the permeability of a single channel (see Fig. 7). A Goldman–Hodgkin–Katz equation is then used to model the open channel current:

$$J_{\mathrm{LCC}} = J_{\mathrm{L}}\delta V \cdot \frac{[\mathrm{Ca}^{2+}]_{\mathrm{o}}e^{-\delta V} - [\mathrm{Ca}^{2+}]_{\mathrm{ds}}}{1-e^{-\delta V}}, \tag{A17}$$

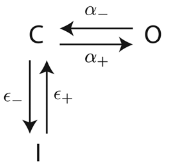

Figure 7. LCC representation
The figure is a schematic representation of the LCC model. There are three possible states, I (inactivated), C (closed) and O (open), with the respective probabilities to move from one state to another α_{+}, α_{-}, ε_{+} and ε_{-}.

where $\delta = zF/RT$, z is the valence for Ca^{2+}, F is the Faraday constant, R is the universal gas constant, T is temperature, J_{L} is the permeability of the channel, V is voltage, and $[\mathrm{Ca}^{2+}]_{\mathrm{o}}$ and $[\mathrm{Ca}^{2+}]_{\mathrm{ds}}$ are respectively external Ca^{2+} and Ca^{2+} in the dyadic space. It must be noted that $[\mathrm{Ca}^{2+}]_{\mathrm{ds}}$ is evaluated using the rapid equilibrium approximation:

$$[\mathrm{Ca}^{2+}]_{\mathrm{ds}} \cong [\mathrm{Ca}^{2+}]_{\mathrm{i}} + \frac{J_{\mathrm{RyR}} + J_{\mathrm{LCC}}}{g_{\mathrm{D}}}, \tag{A18}$$

where J_{RyR} is the current through the rynoadine receptors and g_{D} is the Ca^{2+} flux permeability from the dyadic space to the cytosol. This approximation is one of the crucial steps in the Hinch model simplification (Hinch *et al.* 2004). This yields to the following equation for I_{LCC}:

$$I_{\mathrm{LCC}} = -2J_{\mathrm{LCC}}F\,V_{\mathrm{myouL}}, \tag{A19}$$

where V_{myouL} is the volume of the myocyte in microlitres.

The model, despite its simplifying assumptions, still has nine parameters. We reproduced the peak I_{LCC}–V experiment *in silico* and we performed a sensitivity analysis to evaluate the contribution of each of the nine parameters to the quality of the fit. The experiment was found to be primarily sensitive to the following parameters: V_{L}, the potential when 50% of the LCC channels are open; J_{L}, the permeability of a single channel; and φ_{L}, the proportion of time the channels are still closed but in open mode. In particular the parameters J_{L} and φ_{L} scale the I–V curve while V_{L} determines the slope. We then fitted the parameters to the available experimental data (Fig. 2*A*).

The current through the RyR channels (I_{RYR}) was modelled using the formulation from Hinch *et al.* (2004), a simplified Markovian model of Scheme 6 in Stern *et al.* (1999). The majority of experiments used to parameterize I_{RyR} in Hinch were conducted in isolated SR. This means that they do not capture the process of Ca^{2+}-induced Ca^{2+}-release and are not consistent with our modelling framework (Chu *et al.* 1993; Sitsapesan & Williams, 1994; Mejía-Alvarez *et al.* 1999). The flux through the RyR was modulated to match the experimentally measured time to peak of the Ca^{2+} transients at 1 and 6 Hz. In particular, the half-concentration at activation of the RyR channel (K_{RyR}) was increased from 0.041 to 0.065 mM. It must be noted that we increased the parameter representing the Ca^{2+} flux rate from the dyadic space to the cytosol (g_{D}) from 0.065 $\mu\mathrm{M}^3\ \mathrm{ms}^{-1}$ to 0.099 $\mu\mathrm{M}^3\ \mathrm{ms}^{-1}$ to allow more Ca^{2+} to move between the compartments. This is reasonable as we are dealing with much bigger Ca^{2+} transients than those represented in Pandit *et al.* (2001). In fact, in the Pandit model, the peak of the simulated Ca^{2+} transients approximately spanned from 0.3 μM in the epicardial model to 0.6 μM in the endocardial model. The simulated results were compared with rat experimental traces in Bouchard *et al.* (1995) showing much higher Ca^{2+} transients with peak $\mathrm{Ca}^{2+} \approx 1.2\ \mu$M in normal conditions.

In our model, we took into account the notable increase in peak Ca^{2+} and amplitude by refitting the whole Ca^{2+} dynamic system.

The leak from the SR current I_{SR}: evaluation of $[Ca^{2+}]_{SR}$. During a caffeine transient all Ca^{2+} is released from the SR and it is extruded from the cell via I_{NCX} and I_{PMCa}. There is no change in voltage, and therefore the L-type channels remain in the closed state and SERCA is not pumping Ca^{2+} back to the SR. By integrating the flux of $I_{NCX} + I_{PMCa}$ we can estimate an upper bound on the amount of Ca^{2+} in the SR. Furthermore, during a normal $[Ca^{2+}]_i$ transient, Ca^{2+} is pumped back into the SR by SERCA. At a limit cycle the Ca^{2+} released by the SR must be replaced via SERCA. Integrating I_{SERCA} over a cycle provides a lower bound estimate of the fraction of Ca^{2+} in the SR. With these assumptions we were able to estimate reasonable ranges for $[Ca^{2+}]_{SR}$ at both 1 and 6 Hz: $[Ca^{2+}]_{SR} \in [1.13 \times 10^{-3}, 2.62 \times 10^{-3}]$ mM at 1 Hz and $[Ca^{2+}]_{SR} \in [0.97 \times 10^{-3}, 3.48 \times 10^{-3}]$ mM at 6 Hz. We then scaled the parameter representing the conductivity of the leak SR current, $g_{SRL} = 7.11 \times 10^{-6}\ \mathrm{ms}^{-1}$, in order to keep $[Ca^{2+}]_{SR}$ within these plausible ranges.

The sodium potassium pump (I_{NaK}). In the Pandit model the I_{NaK} formulation was inherited as a variant of the NKA model by Luo & Rudy (1994), developed using a spectrum of different species and temperatures (see Fig. 1*A*). In our model, the current through I_{NaK} was modelled using the formulation from Lewalle *et al.* (2014), directly parameterized from rat data at 37°C:

$$I_{NaK} = I_{NaK_{max}} \cdot \frac{(\gamma + 1)}{\nu_1}, \tag{A20}$$

where

$$\nu_1 = \gamma\left(1 + \frac{K\mathrm{dNaio}}{[\mathrm{Na}^+]_i}\right)^2 \left(1 + \frac{K\mathrm{dNais}}{[\mathrm{Na}^+]_i} e^{\left(-\frac{\delta FVT}{1000R}\right)} + \left(1 + \frac{\alpha}{K\mathrm{e}}\right)^2 \left(1 + \frac{[\mathrm{Na}^+]_o}{K\mathrm{dNaes}} e^{\left(-\frac{(1-\delta)FVT}{1000R}\right)}\right)\right). \tag{A21}$$

The maximum pump rate of I_{NaK} was increased to a value $I_{NaK} = 0.00138\ \mu$A to maintain the intracellular Na^+ gradients within the values found in the literature (see Table 4).

Other K^+ and Na^+ currents. The original Pandit electrophysiology model was fitted to Ca^{2+} data at room temperature and is unable to repolarize sufficiently fast at 6 Hz, causing the model to fail at faster pacing rates. A potential contributor to this particular issue is the transient outward potassium current (I_{to}), which opens immediately after the AP has reached its upstroke and together with the inwardly rectifying K^+ current (I_K) plays a significant role in rat repolarization, shaping the AP (Amin *et al.* 2010; Chae *et al.* 2012). Furthermore, during systole the entrance of Ca^{2+} in the myocyte is driven by the electrical force influenced by I_{to} (Sah *et al.* 2003). In our model, we took into account the notable increase in peak Ca^{2+} and amplitude by refitting the entire Ca^{2+} dynamic system (see Fig. 2) and this inevitably required some major changes in I_{to}. The I_{to} current was tuned to obtain AP repolarization at 6 Hz, maintaining the simulated Ca^{2+} transients. To ensure the AP recovered at higher pacing frequencies we refitted the peak current, activation and recovery rates for I_{to}. With detailed literature research we found I_{to} τ of inactivation values to be much lower in rat experimental data compared with the values used in Pandit (see Table 7). We reduced the values to $\tau_s \approx 50$ ms and $\tau_{sslow} \approx 1100$ ms consistent with values reported by Apkon & Nerbonne (1991) and Varro *et al.* (1993) and $\tau_r \approx 0.01$ ms. This modification significantly improved the ability of the model to repolarize at 6 Hz. The I_{to} peak density was maintained around 2.1 nA at 1 Hz, consistent with the findings in Wickenden *et al.* (1997). Both the equations for I_K and the steady state outward K^+ current (I_{ss}) were kept from Pandit. The I_K conductivity parameter was scaled to a value of $g_{K1} = 4 \times 10^{-5}$ mS to take into account the changes in the I_K current with temperature reported by McLarnon *et al.* (1993) ($Q_{10} = 1.4$ from 10°C to 20°C and $Q_{10} = 1.6$ from 20°C to 30°C). The I_{ss} conductivity parameter was chosen to be $g_{ss} = 1.2 \times 10^{-5}$ mS, to obtain a peak current value equal to the mean value between the epicardial and endocardial Pandit model's peak current measurements. The background K^+ current (I_{BK}) was unchanged. The Na^+ current (I_{Na}) conductivity parameter was fitted to achieve the peak of the AP at 1 Hz. The background Na^+ current (I_{BNa}) and the hyperpolarized activated current (I_f) were unchanged.

Summary of fitted parameters. A summary of all the fitted parameters within the model is shown in Tables 8 and 9.

Simulated Ca^{2+} and AP phenotypes at all tested frequencies for data-driven (DD) model

For the sake of completeness, in Tables 10 and 11 we report the results of all simulated Ca^{2+} and AP phenotypes for all tested frequencies from 1 to 6 Hz with step 1 Hz.

Changes in extracellular potassium concentration

The initial model is parameterized to experimental measurements where $[K^+]_o$ was set to 5.4 mM. However, lower $[K^+]_o$ values between 3.3 and 5.8 mM were reported

Table 7. Summary of I_{to} current measurements reported in the literature

Publication	T (°C)	F (Hz)	Amplitude (nA)	τ_r (ms)	τ_s (ms)	τ_{sslow} (ms)
Apkon & Nerbonne (1991)	23 ± 1	NR	1.4	0.96	41.0 ± 14.5	1238 ± 566
Varro *et al.* (1993)	20–25	0.33			47.4 ± 4.0	1185 ± 102
Wickenden *et al.* (1997)	23 ± 1	1	2.10 ± 0.18		31.7 ± 2.7	
Wickenden *et al.* (1997) (N)	23 ± 1	1	1.01 ± 0.15		64.3 ± 8.8	8216 ± 2396
Pandit *et al.* (2001) (endo)	22–24	1	1.22	0.14	514	2985
Pandit *et al.* (2001) (epi)	22–24	1	2.44	0.14	254	3325
Huang *et al.* (2014)	22–24	0.33	1.67 ± 0.02			

N, neonatal cells; epi, epicardial cells; endo, endocardial cells.

Table 8. Summary of all the fitted Ca^{2+} current parameters

Parameter	Unit	Definition
$g_{\mathrm{NCX}} = 0.0515 \times 10^{-3}$	$\mu M^3\ ms^{-1}$	Pump rate of NCX
$g_{\mathrm{PMCa}} = 0.005 \times 10^{-3}$	$\mu M^3\ ms^{-1}$	Maximum pump rate of sarcolemmal pump
$K_{\mathrm{PMCa}} = 0.35 \times 10^{-3}$	mM	Half-saturation of sarcolemmal pump
$g_{\mathrm{SERCA1}} = 0.47 \times 10^{-3}$	$\mu M^3\ ms^{-1}$	Maximum pump rate of SERCA at 1 Hz
$K_{\mathrm{SERCA1}} = 0.45 \times 10^{-3}$	mM	Half-saturation of SERCA at 1 Hz
$g_{\mathrm{SERCA6}} = 0.68 \times 10^{-3}$	$\mu M^3\ ms^{-1}$	Maximum pump rate of SERCA at 6 Hz
$K_{\mathrm{SERCA6}} = 0.45 \times 10^{-3}$	mM	Half-saturation of SERCA at 6 Hz
$J_{\mathrm{L}} = 7 \times 10^{-4}$	$\mu M^3\ ms^{-1}$	Permeability of single LCC
$K_{\mathrm{L}} = 0.0006$	mM	Concentration at inactivation LCC
$V_{\mathrm{L}} = -9$	mV	Potential when half LCC open
$\delta_{\mathrm{VL}} = 7$	mV	Width of opening potential
$\phi_{\mathrm{L}} = 11.5$	Unitless	Proportion of time closed in open mode LCC
$\tau_{\mathrm{L}} = 1450$	mS	Inactivation time
$K_{\mathrm{RyR}} = 0.065$	mM	Half concentration of activation
$g_{\mathrm{D}} = 0.099$	$\mu M^3\ ms^{-1}$	Permeability of the leak current from the dyadic space
$g_{\mathrm{SRL}} = 7.11 \times 10^{-6}$	ms^{-1}	Rate of leak from the SR to the cytosol
$g_{\mathrm{CaB}} = 5.10875 \times 10^{-8}$	$mM\ mV^{-1}\ ms^{-1}$	Background Ca^{2+} current rate

Table 9. Summary of the $Na^+$and K^+currents parameters

Parameter	Unit	Definition
$g_{\mathrm{t}} = 1.96 \times 10^{-5}$	mS	Transient outward potassium current conductivity
$g_{\mathrm{K1}} = 4 \times 10^{-5}$	mS	Inwardly rectifying current conductivity
$g_{\mathrm{ss}} = 1.2 \times 10^{-5}$	mS	Steady-state outward K^+ current conductivity
$g_{\mathrm{Na}} = 0.0007$	mS	Inward Na^+ current conductivity
$g_{\mathrm{BK}} = 0.000138 \times 10^{-3}$	mS	Background K^+ current conductivity
$g_{\mathrm{BNa}} = 0.00008015 \times 10^{-3}$	mS	Background Na^+ current conductivity

in vivo, as reviewed by Niederer (2013). To test if changes in $[K^+]_o$ could affect our CFR results we have simulated frequency-dependent changes in PCa, DCa, Δ_{MPCa} and $[Ca^{2+}]_{\mathrm{SR}}$ in the base model with $[K^+]_o = 4.2$ mM and $[K^+]_o = 4.5$ mM as shown in Figs 8 and 9, respectively. No major changes in the calcium–frequency behaviour have been reported in these cases.

Fixed AP simulations

To study the effects of changes in AP on the calcium–frequency response, in Fig. 10 we have simulated frequency-dependent changes in PCa, DCa, Δ_{MPCa} and $[Ca^{2+}]_{\mathrm{SR}}$ when clamping the AP to 1 Hz morphology at all frequencies. Compared with the results in the DD model, no major changes in the calcium–frequency behaviour have been reported in this case.

CAMKII alteration of L-type channel and transient outward K^+ current (CAMK model)

CAMKII alteration of I_{LCC}

Previous studies in rats have shown a CAMKII-mediated increase in I_{LCC} magnitude of approximately 10–20% and

Table 10. Simulated Ca^{2+}phenotypes at all tested frequencies

Phenotype	Unit	1 Hz	2 Hz	3 Hz	4 Hz	5 Hz	6 Hz
Peak $[Ca^{2+}]_i$	μM	1.420	1.331	1.314	1.331	1.372	1.439
DCa	μM	0.1056	0.1141	0.1369	0.1663	0.2014	0.2445
RT_{50}	ms	111	80	68	63	60	61
T_{peak}	ms	27	26	25	24	24	25

Table 11. Simulated AP phenotypes at all tested frequencies

Phenotype	Unit	1 Hz	2 Hz	3 Hz	4 Hz	5 Hz	6 Hz
Resting membrane *V*	mV	−83.06	−83.19	−83.26	−83.28	83.24	−83.16
Peak *V*	mV	38.52	37.45	36.03	34.2	31.8	28.8
APD_{20}	ms	2.6	2.6	2.6	2.7	2.9	3.0
APD_{50}	ms	15.7	17	17.6	18.2	19.1	20.6
APD_{70}	ms	33.0	33.3	33.1	33.1	33.6	34.6
APD_{90}	ms	50.6	49.2	48.3	47.9	48	48.9

APD, action potential duration.

accelerated recovery from inactivation (Xiao *et al.* 1994; Guo & Duff, 2006). In accordance with these findings, results in human models by O'Hara *et al.* (2011) have also shown an increase in peak current and faster recovery from inactivation of I_{LCC} when phosphorylated by CAMK. Following those studies, to obtain an increased magnitude and slowed inactivation in the CAMK model, we increased the LCC permeability by 20% and we doubled the τ_L of inactivation. CAMKII activation of the L-type channel was developed using the same approach we have used for CAMKII SERCA activation:

$$J_L = \overline{\Delta_{JL}} \cdot \frac{f_a}{K_{m,JL} + f_a}, \tag{A22}$$

$$\tau_L = \overline{\Delta_\tau} \cdot \frac{f_a}{K_{m,\tau} - f_a}, \tag{A23}$$

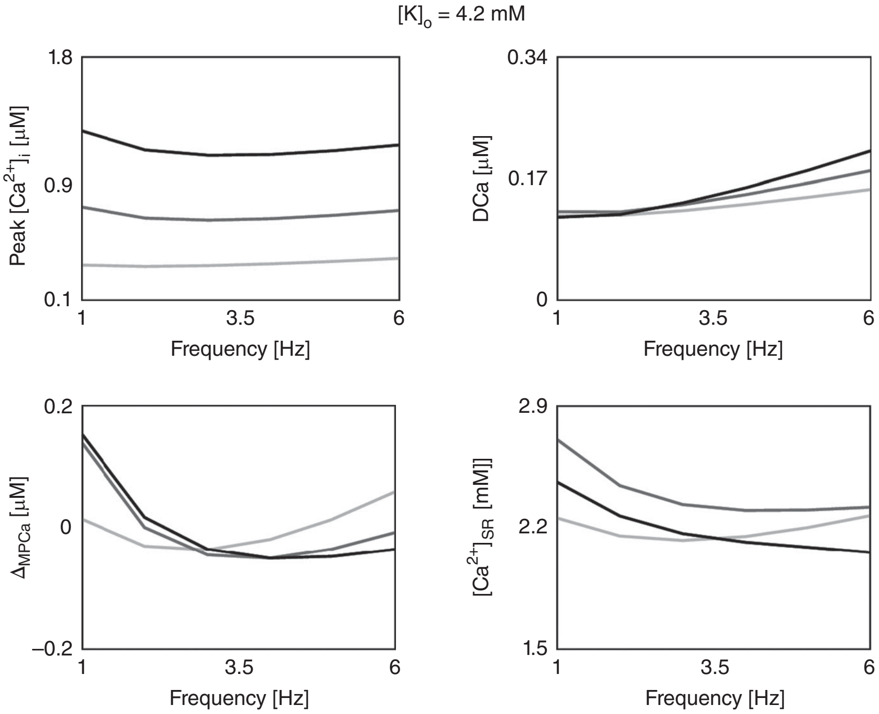

Figure 8. PCa, DCa, Δ_{MPCa} and $[Ca^{2+}]_{SR}$ changes with $[Ca^{2+}]_o$ when $[K^+]_o$ = 4.2 mM
No major changes in the calcium–frequency behaviour have been reported in this case.

where f_a is the fractional occupancies of active CaMKII, $\overline{\Delta_{JL}} = 0.002575$, $K_{m,JL} = 1.72$, $\overline{\Delta_{\tau}} = 1153$ and $K_{m,\tau} = 1.153$. Results in Fig. 11 show an increase in the current magnitude and slowed inactivation comparable with results digitalized from Xiao *et al.* (1994). Interestingly, Dibb *et al.* (2007) found no evidence for frequency-dependent facilitation of I_{LCC} in rat experiments at 37°C and they showed that peak I_{LCC} decreases with increasing stimulation frequency. Consistent with these studies, our DD model shows decreased peak I_{LCC} with increasing frequency as shown in Fig. 12.

CAMK alteration of I_{to}

Experiments by Colinas *et al.* (2006) in rat cardiac myocytes have revealed a direct regulation of the fast I_{to} component by CAMKII. Furthermore, inhibition of CAMKII with KN-93 resulted in acceleration of I_{to} inactivation, thought to be caused by a reduction in the I_{to} slow component with no physiologically significant changes on the constants of inactivation. More recent experiments developed by Wagner *et al.* (2009) in mouse showed that CAMKII does not produce regulation of I_{to} amplitude or activation, although it accelerates recovery from inactivation for both the fast and slow I_{to} components.

Following these studies, in the CAMK model we altered the I_{to} steady state inactivation with a 15 mV shift in the depolarizing direction, to reduce both the fast and the slow inactivating components, and we introduced CAMKII activation of the I_{to} τ of inactivation, to accelerate recovery from inactivation:

$$s_{\text{infinity}} = s\text{slow}_{\text{infinity}} = \frac{1}{\frac{1+e^{(V+\alpha)}}{6.8841}}, \qquad \text{(A24)}$$

$$\alpha = \overline{\Delta_a} \cdot \frac{f_a}{K_a - f_a}, \qquad \text{(A25)}$$

where f_a is the fractional occupancies of active CaMKII, $\overline{\Delta_a} = -14.57$ and $K_a = 0.435$.

$$\tau_s = \beta e^{-\left(\frac{V+70}{25}\right)^2} + \delta, \qquad \text{(A26)}$$

$$\tau_{\text{sslow}} = \gamma e^{-\left(\frac{V+70}{30}\right)^2} + \delta, \qquad \text{(A27)}$$

$$\beta = \overline{\Delta_b} \cdot \frac{f_a}{K_b - f_a}, \qquad \text{(A28)}$$

$$\gamma = \overline{\Delta_g} \cdot \frac{f_a}{K_g + f_a}, \qquad \text{(A29)}$$

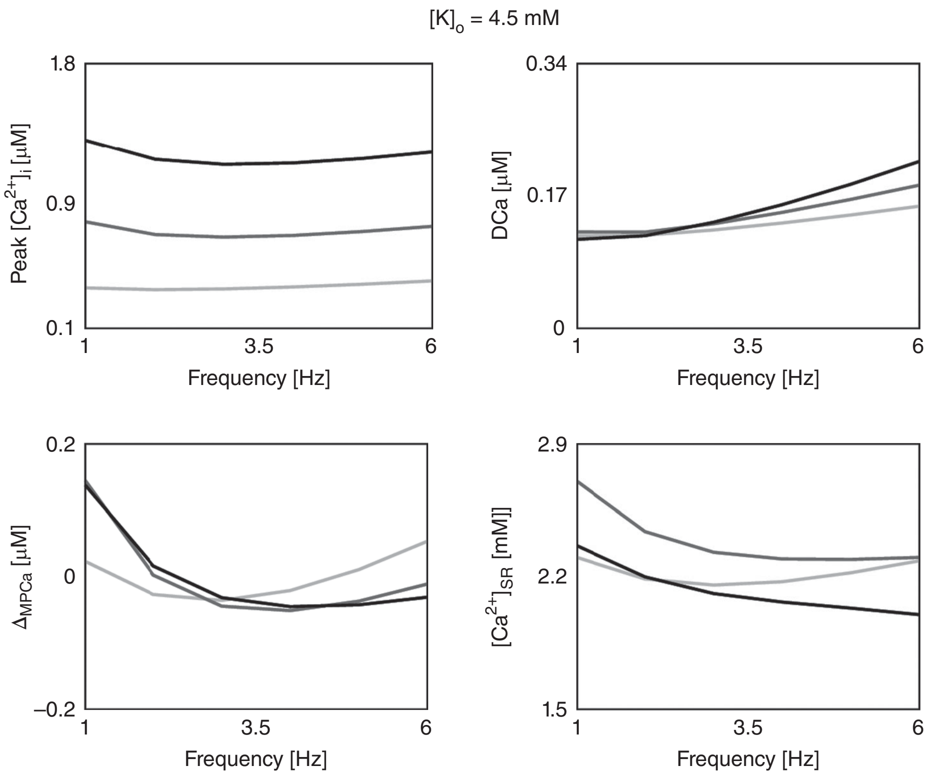

Figure 9. PCa, DCa, Δ_{MPCa} and $[Ca^{2+}]_{SR}$ changes with $[Ca^{2+}]_o$ when $[K^+]_o = 4.5$ mM
No major changes in the calcium–frequency behaviour have been reported in this case.

$$\delta = \overline{\Delta_{\mathrm{d}}} \cdot \frac{f_{\mathrm{a}}}{K_{\mathrm{d}} + f_{\mathrm{a}}}, \qquad \text{(A30)}$$

where $\overline{\Delta_{\mathrm{b}}} = 14.87$, $K_{\mathrm{b}} = 1.118$, $\overline{\Delta_{\mathrm{g}}} = 3069$, $K_{\mathrm{g}} = 0.8757$, $\overline{\Delta_{\mathrm{d}}} = 19.9$ and $K_{\mathrm{d}} = 1.007$. Results in Fig. 13 show slowed I_{to} inactivation compared with the DD case and no changes in I_{to} amplitude or activation concordant with results by Colinas *et al.* (2006) and Wagner *et al.* (2009).

Mechanisms behind the CFR in model variants

In our work we have simulated the PCFR, DCFR, MCFR and $[\mathrm{Ca}^{2+}]_{\mathrm{SR}}$ frequency response in the DD model and three model variants: CAMK, NO CAMK and RNaK models (Fig. 3). Here for completeness, we report the frequency-dependent changes in those phenotypes for all

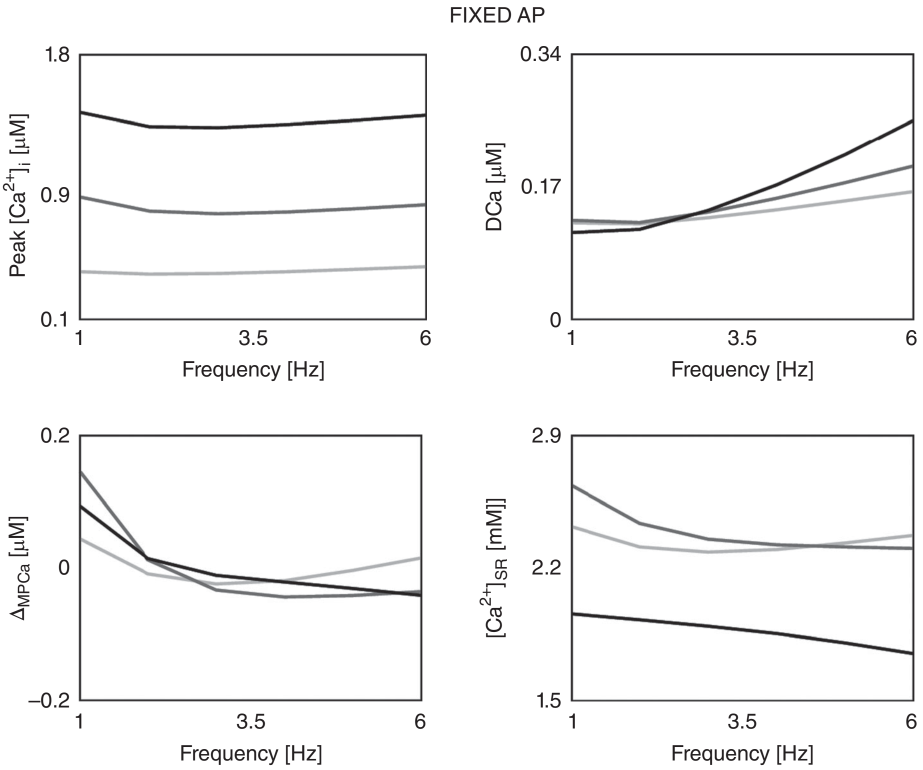

Figure 10. PCa, DCa, Δ_{MPCa} and $[\mathrm{Ca}^{2+}]_{\mathrm{SR}}$ changes with $[\mathrm{Ca}^{2+}]_{\mathrm{o}}$ when fixing the AP to 1 Hz morphology
No major changes in the calcium–frequency behaviour have been reported in this case.

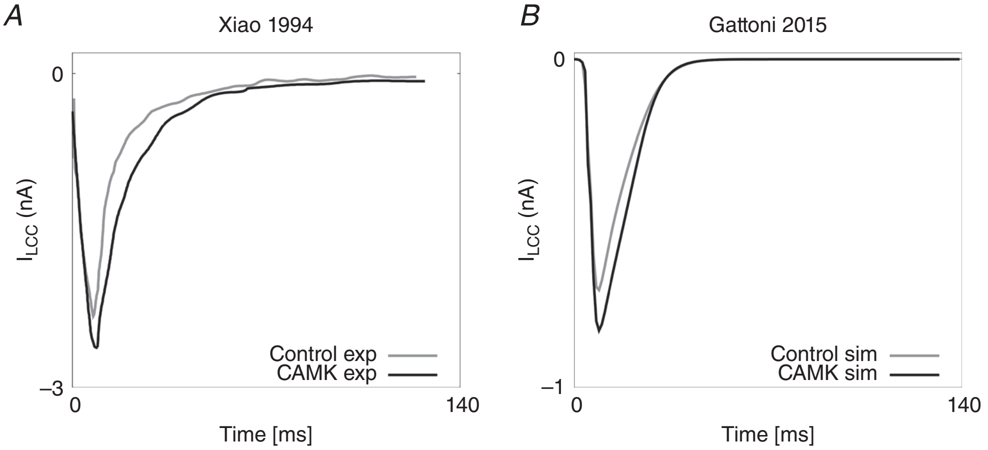

Figure 11. LCC experimental data and simulations
A, I_{LCC} experimental current data in control (grey) and CAMK (black) cases, digitalized from Xiao *et al.* (1994). *B*, I_{LCC} simulated current in control (grey) and CAMK (black) cases in our model.

model variants (in Table 12) and we describe the effects of model variants on the CFR.

CAMK model

In the CAMK model, we introduced equations for CAMKII-mediated LCC and I_{to} activity and tested how this mechanism affected the CFR. Note that CAMK SERCA modulation is also modelled in the CAMK model, as it is already included in the DD model. Table 12 shows that the PCFR in the CAMK model is qualitatively the same as that of the DD model, although we report a positive PCFR at $[Ca^{2+}]_o = 1.8$ mM. In the CAMK model the MCFR is biphasic at $[Ca^{2+}]_o = 1.0$ and 1.4 mM; however, compared with the DD model we see an increased positive staircase for higher frequencies and a shift of the turning point to lower frequencies. MCFR is positive at $[Ca^{2+}]_o = 1.8$ mM.

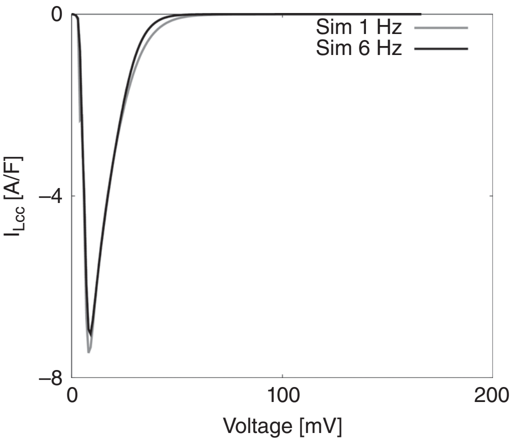

Figure 12. I_{LCC} simulations in the DD model at 1 Hz (grey) and 6 Hz (black)
Results show decreased peak I_{LCC} with increasing frequency.

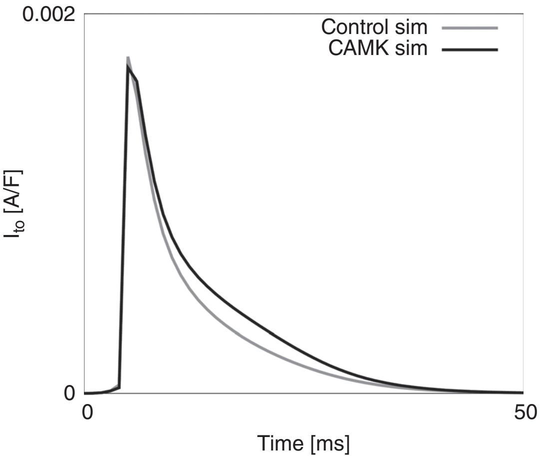

Figure 13. I_{to} current in control and CAMK cases
I_{to} simulated data in control (grey) and CAMK (black) cases. Results show slower inactivation of the I_{to} current when including the effects of CAMKII compared with the control case.

Following the same approach we have used for the DD model, to observe how single fluxes affect the CFR, we simulated the changes in all Ca^{2+} fluxes with $[Ca^{2+}]_o$ and frequency in two cases: with and without rapid calmodulin buffering. Simulation results in Fig. 14 reveal the same mechanism already presented for the DD model in 'Discussion, The $[Ca^{2+}]_{SR}$ hypothesis and analysis of the intracellular and extracellular fluxes behind CFR'. The PCFR is mainly driven by the RyR flux, with a clear effect of the rapid calmodulin buffer and DCa on the response, especially at high levels of $[Ca^{2+}]_o$. We report biphasic RyR response with frequency at all values of $[Ca^{2+}]_o$. The biphasic RyR explains the biphasic PCFR at $[Ca^{2+}]_o = 1.0$ and 1.4 mM. The positive PCFR staircase at $[Ca^{2+}]_o = 1.8$ mM only appears when the effect of the rapid calmodulin buffer is included in the integrals evaluation, showing the clear role of the buffering system in shaping the PCFR response. These results show that CAMKII-mediated activity, directly acting on Ca^{2+} release from the RyR, enhances the positive MCFR staircase.

NO CAMK model

In the NO CAMK model, we inhibited CAMKII up-regulation of SERCA with frequency to observe the effects on the CFR, by fixing the SERCA conductivity parameter to its value at 6 Hz. Fixing SERCA conductivity at 1 Hz resulted in alternans for frequencies > 4 Hz. Results of the NO CAMK model in Table 12 reveal that removal of SERCA CAMKII dependency mainly affects the PCFR and MCFR. Compared with the biphasic behaviour in the DD model, the NO CAMK model shows a flattened PCFR staircase and a negative MCFR in all cases. In Fig. 15 we observed how single fluxes affect the CFR by simulating the changes in all Ca^{2+} fluxes with $[Ca^{2+}]_o$ and frequency in two cases: with and without rapid calmodulin buffering. Compared with the DD model, where we saw increased SERCA activity with frequency, in the NO CAMK model we report a decrease in SERCA flux with frequency from 1 to 5 Hz and a slight increase from 5 to 6 Hz which in turn modulates the $[Ca^{2+}]_{SR}$ and the RyR flux. In the NO CAMK model the flattened RyR flux is mainly responsible for the PCFR staircase and we see the effect of the frequency-dependent increase in DCa, inducing a shift to a positive PCFR at high frequencies. In particular, in Fig. 8 we see a notable increase in $[Ca^{2+}]_{SR}$ at low frequencies in the NO CAMK model compared with the DD model, which in turn activates more Ca^{2+} release from the RyR. Compared with the RyR flux in the DD model, in the NO CAMK model we report more Ca^{2+} flux at low frequencies and less Ca^{2+} flux at high frequencies leading to an increase in $[Ca^{2+}]_i$ at low frequencies and

Table 12. PCFR, DCFR, MCFR and $[Ca^{2+}]_{SR}$ frequency relationship ($[Ca^{2+}]_{SR}$ FR) for the DD, CAMK, NO CAMK and RNaK models

		DD MODEL		CAMK MODEL		NO CAMK MODEL		RNaK MODEL	
Phenotype	$[Ca^{2+}]$ (mM)	Negative	Positive	Negative	Positive	Negative	Positive	Negative	Positive
PCFR	1.0	1–2 Hz	2–6 Hz	1–2 Hz	2–6 Hz	1–4 Hz	4–6 Hz	1–2 Hz	2–6 Hz
	1.4	1–3 Hz	3–6 Hz	1–2 Hz	2–6 Hz	1–5 Hz	5–6 Hz	1–2 Hz	2–6 Hz
	1.8	1–3 Hz	3–6 Hz		1–6 Hz	1–4 Hz	4–6 Hz	1–2 Hz	2–6 Hz
	1.0		1–6 Hz		1–6 Hz	1–2 Hz	2–6 Hz		l–6 Hz
DCFR	1.4		1–6 Hz		1–6 Hz		1–6 Hz		l–6 Hz
	1.8		1–6 Hz		1–6 Hz		1–6 Hz		l–6 Hz
	1.0	1–3 Hz	3–6 Hz	1–2 Hz	2–6 Hz	1–6 Hz		1–2 Hz	2–6 Hz
MCFR	1.4	1–4 Hz	4–6 Hz	1–3 Hz	3–6 Hz	1–6 Hz		1–2 Hz	2–6 Hz
	1.8	1–4 Hz	4–6 Hz		1–6 Hz	1–6 Hz		1–3 Hz	3–6 Hz
	1.0	1–3 Hz	3–6 Hz	l–4 Hz	4–6 Hz	1–6 Hz		1–2 Hz	2–6 Hz
$[Ca^{2+}]_{SR}$FR	1.4	1–6 Hz		1–6 Hz		1–6 Hz		1–3 Hz	3–6 Hz
	1.8	1–6 Hz		1–6 Hz		1–6 Hz		1–2 Hz	2–6 Hz

a decrease in $[Ca^{2+}]_i$ at high frequencies, responsible for the negative MCFR. These results show that CAMK up-regulated SERCA modulates the shift from negative to positive PCFR by altering the $[Ca^{2+}]_{SR}$, inducing changes in the RyR frequency response.

It could be argued that pinning SERCA to its 6 Hz value does not appear to correspond with inhibition but rather over-expression of CaMKII, since SERCA would presumably be less active at slower rates. Thus for the sake of completeness, we performed the same simulations in the range 1–4 Hz by fixing the SERCA conductivity parameter at 1 Hz. Results in Fig. 16 do not show relevant changes in the PCFR, DCFR and MCFR in this case.

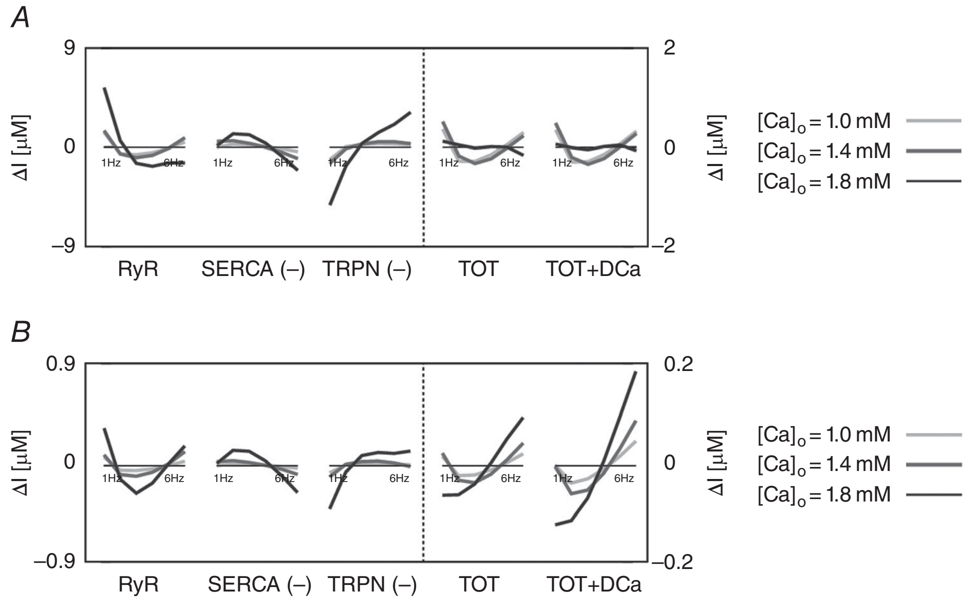

Figure 14. Integral variations in the CAMK model
CAMK model intracellular and extracellular current variation of integrals (ΔI) as a function of frequency (1 to 6 Hz). *A*, CAMK model without buffer. *B*, CAMK model with buffer. In both cases the integrals were evaluated from time = 0 to time = T_{peak}, where T_{peak} is the time to peak of the corresponding simulated Ca^{2+} transient. Colours represent different extracellular Ca^{2+} concentrations: 1.0 mM (light grey), 1.4 mM (dark grey) and 1.8 mM (black). The most important fluxes, plotted in the figure, are ryanodine receptors (RyR), Ca^{2+}-ATPase (SERCA), troponin buffer (TRPN), total current (TOT) and total current plus diastolic Ca^{2+} (TOT+DCa). The other observed fluxes, L-type Ca^{2+} channel (LCC), background Ca^{2+} current (CaB), reverse mode Na^+/Ca^{2+} exchanger (NCXR), forward mode Na^+/Ca^{2+} exchanger (NCXF), Ca^{2+} pump (PMCa) and SR leak current (SRl) were one or more orders of magnitude smaller, and therefore we did not include them in the figure.

RNaK model

In the RNaK model we reduced the Na^+/K^+ affinity to Na^+ to test the effects on the CFR. Results of the RNaK model in Table 12 show a shift of the turning point of the biphasic PCFR and MCFR responses to lower frequencies compared with the DD model. We report reduced $[Na^+]_i$ for frequencies < 2 or 3 Hz and augmented $[Na^+]_i$ for frequencies > 2 or 3 Hz depending on $[Ca^{2+}]_o$. In particular, at $[Ca^{2+}]_o = 1.8$ mM, we report an $[Na^+]_i$ increase of ∼10% at 3 Hz and ∼30% at 6 Hz.

To observe how single fluxes affect the CFR in the RNaK model, in Fig. 17 we simulated the changes in all Ca^{2+} fluxes with $[Ca^{2+}]_o$ and frequency in two cases: with and without rapid calmodulin buffering. As NCX kinetics are

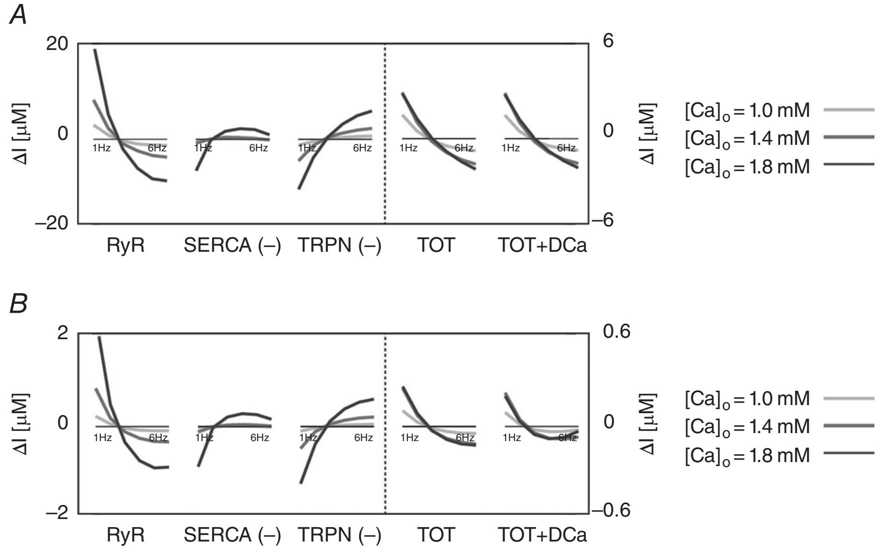

Figure 15. Integral variations in the NO CAMK model
NO CAMK model intracellular and extracellular current variation of integrals (ΔI) as a function of frequency (1 to 6 Hz). *A*, NO CAMK model without buffer. *B*, NO CAMK model with buffer. In both cases the integrals were evaluated from time = 0 to time = T_{peak}, where T_{peak} is the time to peak of the correspondent simulated Ca^{2+} transient. Colours represent different extracellular Ca^{2+} concentrations: 1.0 mM (light grey), 1.4 mM (dark grey) and 1.8 mM (black). The most important fluxes, plotted in figure, are ryanodine receptors (RyR), Ca^{2+}-ATPase (SERCA), troponin buffer (TRPN), total current (TOT) and total current plus diastolic Ca^{2+} (TOT+DCa). The other observed fluxes, L-type Ca^{2+} channel (LCC), background Ca^{2+} current (CaB), reverse mode Na^+/Ca^{2+} exchanger (NCXR), forward mode Na^+/Ca^{2+} exchanger (NCXF), Ca^{2+} pump (PMCa) and SR leak current (SRl) were one or more orders of magnitude smaller, and therefore we did not include them in the figure.

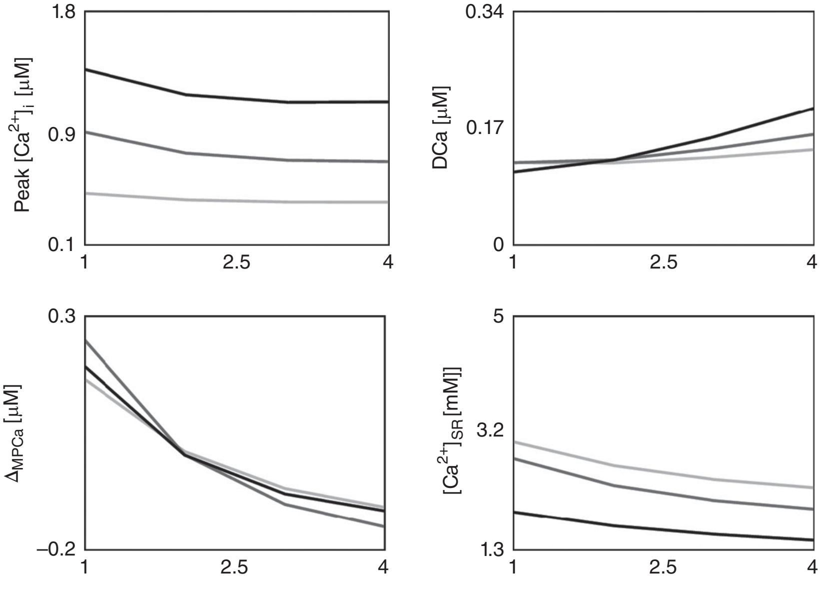

Figure 16. Ca^{2+} phenotype changes with $[Ca^{2+}]_o$ when inhibiting CAMKII up-regulation of SERCA with frequency, by fixing the SERCA conductivity parameter to its value at 1 Hz
Results do not show main changes in the CFR response.

dependent on $[\mathrm{Na}^+]_i$ and $[\mathrm{Ca}^{2+}]_i$, at lower $[\mathrm{Na}^+]_i$ levels (i.e. at lower frequencies), NCX operates less in reverse mode and more in forward mode inducing a reduction in $[\mathrm{Ca}^{2+}]_i$, in the RNaK model compared with the DD model. Conversely at higher $[\mathrm{Na}^+]_i$ levels (i.e. at higher frequencies) NCX operates more in reverse mode and less in forward mode inducing an increase in $[\mathrm{Ca}^{2+}]_i$ in the RNaK model compared with the DD model. Changes in $[\mathrm{Ca}^{2+}]_i$ are sensed by the RyR. Compared with the RyR flux in the DD model, in the RNaK model at $[\mathrm{Ca}^{2+}]_o = 1.0$ and 1.4 mM we report less Ca^{2+} flux at low frequency and more Ca^{2+} flux at high frequencies leading to a reduction in $[\mathrm{Ca}^{2+}]_i$ at low frequency and an increase in $[\mathrm{Ca}^{2+}]_i$ at high frequencies, responsible for the enhanced positive MCFR in this model (Fig. 17). At $[\mathrm{Ca}^{2+}]_o = 1.8$ mM, we report a decrease in the RyR flux with frequency, due to the very high increase in DCa, which leads to a decrease in SERCA flux with frequency. Results at $[\mathrm{Ca}^{2+}]_o = 1.8$ mM still show enhanced biphasic MCFR response due to the lower $[\mathrm{Ca}^{2+}]_i$ levels at low frequency in the RNaK compared with the DD model. The RNaK model biphasic PCFR response reveals the same mechanism as demonstrated in the DD model in 'Discussion, The $[\mathrm{Ca}^{2+}]_{\mathrm{SR}}$ hypothesis and analysis of the intracellular and extracellular fluxes behind CFR'. When $[\mathrm{Ca}^{2+}]_o < 1.8$ mM, the biphasic PCFR staircase is due to the biphasic RyR flux, amplified by the rapid buffering system and DCa as shown in Fig. 17. At $[\mathrm{Ca}^{2+}]_o = 1.8$ mM the RyR staircase results are negative with frequency. Here the biphasic PCFR staircase only appears when the rapid buffering coefficient is included in the simulation, revealing the importance of the buffering system in the PCFR staircase. Decreasing the $\mathrm{Na}^+/\mathrm{K}^+$ affinity to Na^+, our model shows positive PCFR and MCFR for frequencies > 2 or 3 Hz depending on $[\mathrm{Ca}^{2+}]_o$, highlighting the role of $[\mathrm{Na}^+]_i$ in enhancing the positive staircase effect at physiological frequencies.

Intracellular and extracellular fluxes in the CAMK, NO CAMK and RNaK models

Changes in CFR with alterations in $[\mathrm{Ca}^{2+}]_o$ are due to changes in the balance of Ca^{2+} fluxes and the degree of buffered Ca^{2+}. For the sake of completeness, in Figs 14, 15 and 17 we show the variation of the integrals of fluxes with changes in $[\mathrm{Ca}^{2+}]_o$ and frequency in the CAMK, NO CAMK and RNaK models, respectively.

Limitations

The choice of performing experiments at 37°C, although interesting from the physiological point of view, could

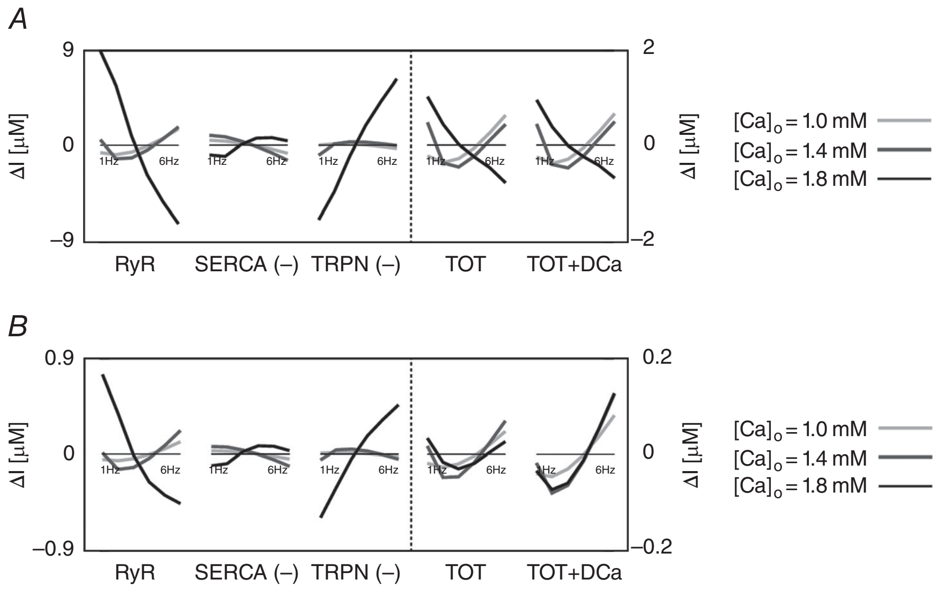

Figure 17. Integral variations in the RNaK model
RNaK model intracellular and extracellular current variation of integrals (ΔI) as a function of frequency (1 to 6 Hz). *A*, RNaK model without buffer. *B*, RNaK model with buffer. In both cases the integrals were evaluated from time = 0 to time = T_{peak} where T_{peak} is the time to peak of the corresponding simulated Ca^{2+} transient. Colours represent different extracellular Ca^{2+} concentrations: 1.0 mM (light grey), 1.4 mM (dark grey) and 1.8 mM (black). The most important fluxes, plotted in the figure, are ryanodine receptors (RyR), Ca^{2+}-ATPase (SERCA), troponin buffer (TRPN), total current (TOT) and total current plus diastolic Ca^{2+} (TOT+DCa). The other observed fluxes, L-type Ca^{2+} channel (LCC), background Ca^{2+} current (CaB), reverse mode $\mathrm{Na}^+/\mathrm{Ca}^{2+}$ exchanger (NCXR), forward mode $\mathrm{Na}^+/\mathrm{Ca}^{2+}$ exchanger (NCXF), Ca^{2+} pump (PMCa) and SR leak current (SRl) were one or more orders of magnitude smaller, and therefore we did not include them in the figure.

represent a limitation in our model as previous literature studies have shown the presence of voltage clamp artifacts when performing experiments at temperatures greater than 30°C. Increasing temperature causes reactions to become faster and it is more difficult to accurately control the clamped voltage. To address this problem, we have used data that have employed low resistance pipettes and a rapid switching frequency, which enables improved voltage control. These methods are considered to be widely employed and reliable.

In our experiments we have used $[\mathrm{Ca}^{2+}]_o = 1.8$ mM and $[\mathrm{K}^+]_o = 5.4$ mM. This choice represents a limitation, as the concentration of free calcium in rat plasma remains contentious. Previous studies have measured the extracellular free calcium concentration to be between 1 and 1.3 mM in rats (Moore, 1970; Polimeni, 1974) and the plasma concentrations of potassium to be between 3.3 and 5.8 mM, as reviewed in Niederer (2013). Our simulated results are consistent with the experimental data at $[\mathrm{Ca}^{2+}]_o = 1.8$ mM and $[\mathrm{K}^+]_o = 5.4$ mM and we predicted how changes in $[\mathrm{Ca}^{2+}]_o$ affect the CFR response in our model. To study the effects of changes in $[\mathrm{K}^+]_o$ concentration on the calcium–frequency response, in Figs 8 and 9 we have simulated frequency-dependent changes in PCa, DCa, Δ_{MPCa} and $[\mathrm{Ca}^{2+}]_{\mathrm{SR}}$ in the base model with $[\mathrm{K}^+]_o = 4.2$ mM and $[\mathrm{K}^+]_o = 4.5$ mM and we have shown that those do not affect the conclusions of our work.

The interplay between calcium, TnC and tension generation is not included in our analysis and represents a limitation in our model. The inclusion of a sarcomere model with tension-dependent Ca^{2+} buffering feedback would address this, albeit with a significant increase in model complexity. However, due to the relative timing of the tension and the Ca^{2+} transient, the largest effect of tension-dependent buffering will occur during the relaxation of the Ca^{2+} transient with limited impact on the peak or magnitude of the Ca^{2+} transient.

Another important consideration is the significant variability of data. Our computer model is deterministic and thus contrasts sharply with the high levels of intra- and intermyocyte variability in action potentials and Ca^{2+} transient measurements. The challenge of interpreting the experimental results is further compounded by the uncoupled measurement of action potential and Ca^{2+} transients. It is also not known which action potential pairs with which Ca^{2+} transient. This lack of information on covariation of data and high variability motivated us to fit the model to representative traces.

The parameters describing the SR geometry and Ca^{2+} buffering represent a limitation in our model. The SR geometry parameters are assumed to be temperature independent and were thus maintained unchanged from the Hinch model (Hinch *et al.* 2004) based on data in canine ventricular myocytes (Greenstein & Winslow, 2002). Interestingly, Page *et al.* found the SR volume to be 3.5% of the cell volume (Page *et al.* 1971; Page, 1978) in rats, slightly lower than the value used in our model. We tested how such a reduction could affect the results and we found no qualitative or quantitative change in the Ca^{2+} transient characteristics. Buffering remains an important but poorly experimentally characterized property of cardiac myocytes, in part due to the need to measure both voltage and calibrated free calcium to characterize the steady state properties of the system. Bers (2001) found that these parameters did not vary significantly between measurements when averaged, although buffering in individual myocytes has been reported to vary significantly (Hove-Madsen & Bers, 1993). The current data are derived from ferret and canine measurements (Greenstein & Winslow, 2002; Bondarenko *et al.* 2004).

Changes in action potential duration might also contribute to FFR (Endoh, 2004), although they appear to be a consequence of changes in $[\mathrm{Ca}^{2+}]_i$. To observe how changes in AP could affect the CFR, we clamped the AP to 1 Hz morphology when simulating at different frequencies. Figure 10 shows that no major changes in the CFR response were detected.

In our experimental data set, AP early repolarization, recorded at 6 Hz, is very different among different cells. Furthermore, the early repolarization phase of the AP appears to be faster in some of the experiments compared with our model's predictions. There are a number of possible reasons for this. One reason could be due to changes in the I_{to} current in different cell types (epicardial/endocardial) that where not accounted for in the model and could explain this variation in AP early repolarization (Fedida & Giles, 1991; Clark *et al.* 1993). Another reason could be due to the fact that AP measurements were recorded in the presence of a small but significant EGTA calcium buffer concentration. The shape of the AP is definitely altered by changes in the intracellular calcium concentration, especially in the early repolarization phase and the presence of a calcium buffer during the experimental recording phase could alter the AP measurements. The effects of changes in EGTA concentration were included when simulating AP in our model although the EGTA model was not re-parameterized for experiments in rats at 37°C. Furthermore, it is not known which AP pairs with which Ca^{2+} transient. This can be a problem, due to the very high variability of the Ca^{2+} experimental data.

References

Amin AS, Tan HL & Wilde AAM (2010). Cardiac ion channels in health and disease. *Heart Rhythm* **7**, 117–126.

Apkon M & Nerbonne JM (1991). Characterization of two distinct depolarization-activated K^+ currents in isolated adult rat ventricular myocytes. *J Gen Physiol* **97**, 973–1011.

Bassani RA, Bassani JW & Bers DM (1992). Mitochondrial and sarcolemmal Ca^{2+} transport reduce $[Ca^{2+}]_i$ during caffeine contractures in rabbit cardiac myocytes. *J Physiol* **453**, 591–608.

Baartscheer A, Schumacher CA & Fiolet JW (1997). Small changes of cytosolic sodium in rat ventricular myocytes measured with SBFI in emission ratio mode. *J Mol Cell Cardiol* **29**, 3375–3383.

Benforado JM (1958). Frequency-dependent pharmacological and physiological effects on the rat ventricle strip. *J Pharmacol Exp Ther* **122**, 86–100.

Bers DM (1989). SR Ca loading in cardiac muscle preparations based on rapid-cooling contractures. *Am J Physiol Cell Physiol* **256**, C109–C120.

Bers DM (2001). *Excitation-Contraction Coupling and Cardiac Contractile Force.* Springer Netherlands, Dordrecht. Available at: http://link.springer.com/10.1007/978-94-010-0658-3 (Accessed 21 April 2015).

Blayney L, Thomas H, Muir J & Henderson A (1978). Action of caffeine on calcium transport by isolated fractions of myofibrils, mitochondria, and sarcoplasmic reticulum from rabbit heart. *Circ Res* **43**, 520–526.

Bondarenko VE, Bett GC & Rasmusson RL (2004). A model of graded calcium release and L-type Ca^{2+} channel inactivation in cardiac muscle. *Am J Physiol Heart Circ Physiol* **286**, H1154–H1169.

Borzak S, Murphy S & Marsh JD (1991). Mechanisms of rate staircase in rat ventricular cells. *Am J Physiol Heart Circ Physiol* **260**, H884–H892.

Borzak S, Reers M, Arruda, J, Sharma VK, Sheu SS, Smith TW & Marsh JD (1992). Na+ efflux mechanisms in ventricular myocytes: measurement of [Na+]i with Na(+)-binding benzofuran isophthalate. *Am J Physiol* **263**, H866–H874.

Bouchard RA & Bose D (1989). Analysis of the interval-force relationship in rat and canine ventricular myocardium. *Am J Physiol Heart Circ Physiol* **257**, H2036–H2047.

Bouchard RA, Clark RB & Giles WR (1995). Effects of action potential duration on excitation-contraction coupling in rat ventricular myocytes. Action potential voltage-clamp measurements. *Circ Res* **76**, 790–801.

Capogrossi MC, Kort AA, Spurgeon HA & Lakatta EG (1986). Single adult rabbit and rat cardiac myocytes retain the Ca^{2+}- and species-dependent systolic and diastolic contractile properties of intact muscle. *J Gen Physiol* **88**, 589–613.

Chae JE, Kim HS, Ahn DS & Park WK (2012). Ionic mechanisms of desflurane on prolongation of action potential duration in rat ventricular myocytes. *Yonsei Med J* **53**, 204–212.

Cheng H, Lederer WJ & Cannell MB (1993). Calcium sparks: elementary events underlying excitation-contraction coupling in heart muscle. *Science* **262**, 740–744.

Choi HS & Eisner DA (1999). The effects of inhibition of the sarcolemmal Ca-ATPase on systolic calcium fluxes and intracellular calcium concentration in rat ventricular myocytes. *Pflugers Arch* **437**, 966–971.

Chu A, Fill M, Stefani E & Entman ML (1993). Cytoplasmic Ca^{2+} does not inhibit the cardiac muscle sarcoplasmic reticulum ryanodine receptor Ca^{2+} channel, although Ca^{2+}-induced Ca^{2+} inactivation of Ca^{2+} release is observed in native vesicles. *J Membr Biol* **135**, 49–59.

Clark RB, Bouchard RA, Salinas-Stefanon E, Sanchez-Chapula J & Giles WR (1993). Heterogeneity of action potential waveforms and potassium currents in rat ventricle. *Cardiovasc Res* **27**, 1795–1799.

Cohen CJ, Fozzard HA & Sheu SS (1982). Increase in intracellular sodium ion activity during stimulation in mammalian cardiac muscle. *Circ Res* **50**, 651–662.

Colinas O, Gallego M, Setien R, Lopez-Lopez JR, Perez-Garcia MT & Casis O (2006). Differential modulation of Kv4.2 and Kv4.3 channels by calmodulin-dependent protein kinase II in rat cardiac myocytes. *Am J Physiol Hear Circ Physiol* **291**, H1978–H1987.

Dibb KM, Eisner DA & Trafford AW (2007). Regulation of systolic $[Ca^{2+}]_i$ and cellular Ca^{2+} flux balance in rat ventricular myocytes by SR Ca^{2+}, L-type Ca^{2+} current and diastolic $[Ca^{2+}]_i$. *J Physiol* **585**, 579–592.

Donoso P, Mill JG, Oneill SC & Eisner DA (1992). Fluorescence Measurements of Cytoplasmic and Mitochondrial Sodium Concentration in Rat Ventricular Myocytes. *J Physiol-London* **448**, 493–509.

Drummond GB (2009). Reporting ethical matters in *The Journal of Physiology*: standards and advice. *J Physiol* **587**, 713–719.

Endoh M (2004). Force-frequency relationship in intact mammalian ventricular myocardium: Physiological and pathophysiological relevance. *Eur J Pharmacol* **500**, 73–86.

Fabiato A & Fabiato F (1979). Calcium and cardiac excitation-contraction coupling. *Annu Rev Physiol* **41**, 473–484.

Fedida D & Giles WR (1991). Regional variations in action potentials and transient outward current in myocytes isolated from rabbit left ventricle. *J Physiol* **442**, 191–209.

Frampton JE, Harrison SM, Boyett MR & Orchard CH (1991*a*). Ca^{2+} and Na^+ in rat myocytes showing different force-frequency relationships. *Am J Physiol Cell Physiol* **261**, C739–C750.

Frampton JE, Orchard CH & Boyett MR (1991*b*). Diastolic, systolic and sarcoplasmic reticulum $[Ca^{2+}]$ during inotropic interventions in isolated rat myocytes. *J Physiol* **437**, 351–375.

Frisk M, Koivumäki JT, Norseng PA, Maleckar MM, Sejersted OM & Louch WE (2014). Variable t-tubule organization and Ca^{2+} homeostasis across the atria. *Am J Physiol Heart Circ Physiol* **307**, H609–H620.

Greenstein JL & Winslow RL (2002). An integrative model of the cardiac ventricular myocyte incorporating local control of Ca^{2+} release. *Biophys J* **83**, 2918–2945.

Guo J & Duff HJ (2006). Calmodulin kinase II accelerates L-type Ca^{2+} current recovery from inactivation and compensates for the direct inhibitory effect of $[Ca^{2+}]_i$ in rat ventricular myocytes. *J Physiol* **574**, 509–518.

Hagemann D, Kuschel M, Kuramochi T, Zhu W, Cheng H & Xiao RP (2000). Frequency-encoding Thr17 phospholamban phosphorylation is independent of Ser16 phosphorylation in cardiac myocytes. *J Biol Chem* **275**, 22532–22536.

Harrison SM, McCall E & Boyett MR (1992). The relationship between contraction and intracellular sodium in rat and guinea-pig ventricular myocytes. *J Physiol* **449**, 517–550.

Herrmann-Frank A, Lüttgau HC & Stephenson DG (1999). Caffeine and excitation-contraction coupling in skeletal muscle: a stimulating story. *J Muscle Res Cell Motil* **20**, 223–237.

Hinch R, Greenstein JL, Tanskanen AJ, Xu L & Winslow RL (2004). A simplified local control model of calcium-induced calcium release in cardiac ventricular myocytes. *Biophys J* **87**, 3723–3736.

Hobai IA & Levi AJ (1999). Coming full circle: membrane potential, sarcolemmal calcium influx and excitation-contraction coupling in heart muscle. *Cardiovasc Res* **44**, 477–487.

Hove-Madsen L & Bers DM (1993). Passive Ca buffering and SR Ca uptake in permeabilized rabbit ventricular myocytes. *Am J Physiol Cell Physiol* **264**, C677–C686.

Huang ZB, Fang C, Lin MH, Yuan GY, Zhou SX & Wu W (2014). Effect of fosinopril on the tran- sient outward potassium current of hypertrophied left ventricular myocardium in the spontaneously hypertensive rat. *Naunyn-Schmiedeberg's Arch of Pharmacol* **387**, 419–425. URL: http://www.ncbi.nlm.nih.gov/pubmed/24441766, doi:10.1007/s00210-014-0956-6.

Huke S & Bers DM (2007). Temporal dissociation of frequency-dependent acceleration of relaxation and protein phosphorylation by CaMKII. *J Mol Cell Cardiol* **42**, 590–599.

Hund TJ & Rudy Y (2004). Rate dependence and regulation of action potential and calcium transient in a canine cardiac ventricular cell model. *Circulation* **110**, 3168–3174.

Jafri MS, Rice JJ & Winslow RL (1998). Cardiac Ca^{2+} dynamics: the roles of ryanodine receptor adaptation and sarcoplasmic reticulum load. *Biophys J* **74**, 1149–1168.

Klein MG, Simon BJ & Schneider MF (1990). Effects of caffeine on calcium release from the sarcoplasmic reticulum in frog skeletal muscle fibres. *J Physiol* **425**, 599–626.

Koch-Weser J & Blinks JR (1963). The influence of the interval between beats on myocardial contractility. *Pharmacol Rev* **15**, 601–652.

Langer GA, Brady AJ, Tan ST & Serena D (1975). Correlation of the glycoside response, the force staircase, and the action potential configuration in the neonatal rat heart. *Circ Res* **36**, 744–752.

Layland J & Kentish JC (1999). Positive force- and $[Ca^{2+}]_i$-frequency relationships in rat ventricular trabeculae at physiological frequencies. *Am J Physiol Hear Circ Physiol* **276**, H9–H18.

Levi Aj, Lee CO & Brooksby P (1994). Properties of the fluorescent sodium indicator "SBFI" in rat and rabbit cardiac myocytes. *J Cardiovasc Electrophysiol* **5**, 241–257.

Lewalle A, Niederer SA & Smith NP (2014). Species-dependent adaptation of the cardiac Na^+/K^+ pump kinetics to the intracellular Na^+ concentration. *J Physiol* **592**, 5355–5371.

Li L, Chu G, Kranias EG & Bers DM (1998). Cardiac myocyte calcium transport in phospholamban knockout mouse: relaxation and endogenous CaMKII effects. *Am J Physiol Heart Circ Physiol* **274**, H1335–H1347.

Li L, Niederer SA, Idigo W, Zhang YH, Swietach P, Casadei B & Smith NP (2010). A mathematical model of the murine ventricular myocyte: a data-driven biophysically based approach applied to mice overexpressing the canine NCX isoform. *Am J Physiol Heart Circ Physiol* **299**, H1045–H1063.

Lokuta AJ, Rogers TB, Lederer WJ & Valdivia HH (1995). Modulation of cardiac ryanodine receptors of swine and rabbit by a phosphorylation-dephosphorylation mechanism. *J Physiol* **487**, 609–622.

Louch WE, Sheehan KA & Wolska BM (2011). Methods in cardiomyocyte isolation, culture, and gene transfer. *J Mol Cell Cardiol* **51**, 288–298.

Luo CH & Rudy Y (1994). A dynamic model of the cardiac ventricular action potential. II. Afterdepolarizations, triggered activity, and potentiation. *Circ Res* **74**, 1097–1113.

Mackiewicz U & Lewartowski B (2006). Temperature dependent contribution of Ca^{2+} transporters to relaxation in cardiac myocytes: Important role of sarcolemmal Ca^{2+}-ATPase. *J Physiol Pharmacol* **57**, 3–15.

Maier LS, Pieske B & Allen DG (1997). Influence of stimulation frequency on $[Na^+]_i$ and contractile function in Langendorff-perfused rat heart. *Am J Physiol Heart Circ Physiol* **273**, H1246–H1254.

McLarnon JG, Hamman BN & Tibbits GF (1993). Temperature dependence of unitary properties of an ATP-dependent potassium channel in cardiac myocytes. *Biophys J* **65**, 2013–2020.

Meissner G, Rios E, Tripathy A & Pasek DA (1997). Regulation of skeletal muscle Ca^{2+} release channel (ryanodine receptor) by Ca^{2+} and monovalent cations and anions. *J Biol Chem* **272**, 1628–1638.

Mejía-Alvarez R, Kettlun C, Ríos E, Stern M & Fill M (1999). Unitary Ca^{2+} current through cardiac ryanodine receptor channels under quasi-physiological ionic conditions. *J Gen Physiol* **113**, 177–186.

Monasky MM & Janssen PML (2009). The positive force-frequency relationship is maintained in absence of sarcoplasmic reticulum function in rabbit, but not in rat myocardium. *J Comp Physiol B Biochem Syst Environ Physiol* **179**, 469–479.

Moore EW (1970). Ionized calcium in normal serum, ultrafiltrates, and whole blood determined by ion-exchange electrodes. *J Clin Invest* **49**, 318–334.

Mørk HK, Sjaastad I, Sejersted OM & Louch WE (2009). Slowing of cardiomyocyte Ca^{2+} release and contraction during heart failure progression in postinfarction mice. *Am J Physiol Heart Circ Physiol* **296**, H1069–H1079.

Mubagwa K, Lin W, Sipido K, Bosteels S & Flameng W (1997). Monensin-induced reversal of positive force-frequency relationship in cardiac muscle: role of intracellular sodium in rest-dependent potentiation of contraction. *J Mol Cell Cardiol* **29**, 977–989.

Negretti N, O'Neill SC & Eisner DA (1993). The relative contributions of different intracellular and sarcolemmal systems to relaxation in rat ventricular myocytes. *Cardiovasc Res* **27**, 1826–1830.

Niederer S (2013). Regulation of ion gradients across myocardial ischemic border zones: a biophysical modelling analysis. *PLoS One* **8**, e60323.

O'Hara T, Virág L, Varró A & Rudy Y (2011). Simulation of the undiseased human cardiac ventricular action potential: model formulation and experimental validation. *PLoS Comput Biol* **7**, e1002061.

Page E & Page EG (1968). Distribution of ions and water between tissue compartments in the perfused left ventricle of the rat heart. *Circ Res* **22**, 435–446.

Page E (1978). Quantitative ultrastructural analysis in cardiac membrane physiology. *Am J Physiol Cell Physiol* **235**, C147–C158.

Page E, McCallister LP & Power B (1971). Stereological measurements of cardiac ultrastructures implicated in excitation-contraction coupling. *Proc Natl Acad Sci USA* **68**, 1465–1466.

Pandit SV, Clark RB, Giles WR & Demir SS (2001). A mathematical model of action potential heterogeneity in adult rat left ventricular myocytes. *Biophys J* **81**, 3029–3051.

Picht E, DeSantiago J, Huke S, Kaetzel MA, Dedman JR & Bers DM (2007). CaMKII inhibition targeted to the sarcoplasmic reticulum inhibits frequency-dependent acceleration of relaxation and Ca^{2+} current facilitation. *J Mol Cell Cardiol* **42**, 196–205.

Pieske B, Maier LS, Bers DM & Hasenfuss G (1999). Ca^{2+} handling and sarcoplasmic reticulum Ca^{2+} content in isolated failing and nonfailing human myocardium. *Circ Res* **85**, 38–46.

Polimeni PI (1974). Extracellular space and ionic distribution in rat ventricle. *Am J Physiol* **227**, 676–683.

Polimeni PI & Al-Sadir J (1975). Expansion of extracellular space in the nonischemic zone of the infarcted heart and concomitant changes in tissue electrolyte contents in the rat. *Circ Res* **37**, 725–732.

Powell T, Terrar DA & Twist VW (1980). Electrical properties of individual cells isolated from adult rat ventricular myocardium. *J Physiol* **302**, 131–153.

Sah R, Ramirez RJ, Oudit GY, Gidrewicz D, Trivieri MG, Zobel C & Backx PH (2003). Regulation of cardiac excitation-contraction coupling by action potential repolarization: role of the transient outward potassium current (I_{to}). *J Physiol* **546**, 5–18.

Sham JS, Cleemann L & Morad M (1995). Functional coupling of Ca^{2+} channels and ryanodine receptors in cardiac myocytes. *Proc Natl Acad Sci USA* **92**, 121–125.

Shattock MJ, Bers DM (1989). Rat vs. rabbit ventricle: Ca flux and intracellular Na assessed by ion-selective micro-electrodes. *Am J Physiol* **256**, C813–C822.

Shimoni Y, Severson D & Giles W (1995). Thyroid status and diabetes modulate regional differences in potassium currents in rat ventricle. *J Physiol* **488**, 673–688.

Sitsapesan R & Williams AJ (1990). Mechanisms of caffeine activation of single calcium-release channels of sheep cardiac sarcoplasmic reticulum. *J Physiol* **423**, 425–439.

Sitsapesan R & Williams AJ (1994). Gating of the native and purified cardiac SR Ca^{2+}-release channel with monovalent cations as permeant species preparation of SR membrane vesicles. *Biophys J* **67**, 1484–1494.

Song LS, Sham JSK, Stern MD, Lakatta EG & Cheng H (1998). Direct measurement of SR release flux by tracking "Ca^{2+} spikes" in rat cardiac myocytes. *J Physiol* **512**, 677–691.

Sossalla S, Fluschnik N, Schotola H, Ort KR, Neef S, Schulte T, Wittköpper K, Renner A, Schmitto JD, Gummert J, El-Armouche A, Hasenfuss G & Maier LS (2010). Inhibition of elevated Ca^{2+}/calmodulin-dependent protein kinase II improves contractility in human failing myocardium. *Circ Res* **107**, 1150–1161.

Stemmer P & Akera T (1986). Concealed positive force-frequency relationships in rat and mouse cardiac muscle revealed by ryanodine. *Am J Physiol Heart Circ Physiol* **251**, H1106–H1110.

Stern MD, Song LS, Cheng H, Sham JS, Yang HT, Boheler KR & Ríos E (1999). Local control models of cardiac excitation-contraction coupling. A possible role for allosteric interactions between ryanodine receptors. *J Gen Physiol* **113**, 469–489.

Terkildsen JR, Niederer S, Crampin EJ, Hunter P & Smith NP (2008). Using Physiome standards to couple cellular functions for rat cardiac excitation-contraction. *Exp Physiol* **93**, 919–929.

Trafford AW, Díaz ME & Eisner DA (1999). A novel, rapid and reversible method to measure Ca buffering and time-course of total sarcoplasmic reticulum Ca content in cardiac ventricular myocytes. *Pflugers Arch* **437**, 501–503.

Varro A, Negretti N, Hester SB & Eisner DA (1993). An estimate of the calcium content of the sarcoplasmic reticulum in rat ventricular myocytes. *Pflugers Arch* **423**, 158–160.

Wagner S, Hacker E, Grandi E, Weber SL, Dybkova N, Sossalla S, Sowa T, Fabritz L, Kirchhof P, Bers DM & Maier LS (2009). Ca/calmodulin kinase II differentially modulates potassium currents. *Circ Arrhythm Electrophysiol* **2**, 285–294.

Wehrens XHT, Lehnart SE, Reiken SR & Marks AR (2004). Ca^{2+}/calmodulin-dependent protein kinase II phosphorylation regulates the cardiac ryanodine receptor. *Circ Res* **94**, e61–e70.

Wickenden AD, Kaprielian R, Parker TG, Jones OT & Backx PH (1997). Effects of development and thyroid hormone on K^+ currents and K^+ channel gene expression in rat ventricle. *J Physiol* **504**, 271–286.

Winslow RL, Rice J, Jafri S, Marbán E & O'Rourke B (1999). Mechanisms of altered excitation-contraction coupling in canine tachycardia-induced heart failure, II: model studies. *Circ Res* **84**, 571–586.

Woodbury JW (1963). Interrelationships between ion transport mechanisms and excitatory events. *Fed Proc* **22**, 31–35.

Wu Y, Luczak ED, Lee EJ, Hidalgo C, Yang J, Gao Z, Li J, Wehrens XH, Granzier H & Anderson ME (2012). CaMKII effects on inotropic but not lusitropic force frequency responses require phospholamban. *J Mol Cell Cardiol* **53**, 429–436.

Xiao RP, Cheng H, Lederer WJ, Suzuki T & Lakatta EG (1994). Dual regulation of Ca^{2+}/calmodulin-dependent kinase II activity by membrane voltage and by calcium influx. *Proc Natl Acad Sci USA* **91**, 9659–9663.

Additional information

Competing interests

The authors declare there are no competing interests.

Author contributions

S.G. developed the modelling framework, performed the parameter fittings and analysis, and wrote the manuscript. A.T.R, M.F and W.L. acquired the data and assisted in the writing of the manuscript. S.A.N. and N.P.S. contributed to the conception and motivation of the analysis and to the interpretation of the results, and assisted in the writing of the manuscript. All authors approved the final version of the manuscript. All authors agree to be accountable for all aspects of the work in ensuring that questions related to the accuracy or integrity of any part of the work are appropriately investigated and resolved. All persons designated as authors qualify for authorship.

Funding

This work was supported by the Virtual Physiological Rat Project (NIH 1 P50 GM094503-01). The project has also received funding from the European Union's Horizon 2020 research and innovation programme (Consolidator grant, WEL) under grant agreement No 647714, South-Eastern Norway Regional Health Authority, Anders Jahre's Fund for the Promotion of Science, the Norwegian Institute of Public Health, Oslo University Hospital Ullevål, and the University of Oslo.

Acknowledgements

The authors acknowledge financial support from the Department of Health via the National Institute for Health Research (NIHR) comprehensive Biomedical Research Centre award to Guys & St Thomas NHS Foundation Trust in partnership with Kings College London and Kings College Hospital NHS Foundation Trust.